AD-A014 807

EFFECTS OF AIRPLANE FLOWFIELDS ON CLOUD WATER CONTENT MEASUREMENTS

Hillyer G. Norment

Mount Auburn Research Associates, Incorporated

Prepared for:

Air Force Cambridge Research Laboratories

30 April 1975

p.1 DC

268218

AFCRL-TR-75-0231

ADA014807

EFFECTS OF AIRPLANE FLOWFIELDS ON CLOUD WATER CONTENT MEASUREMENTS

Hillyer G. Norment

Mt. Auburn Research Associates, Inc.
381 Elliot Street
Newton, Massachusetts 02164

30 April 1975

Final Report for Period 19 September 1975 - 30 April 1975

AIR FORCE CAMBRIDGE RESEARCH LABORATORIES
AIR FORCE SYSTEMS COMMAND
UNITED STATES AIR FORCE
HANSCOM AFB, MASSACHUSETTS 01731

Qualified requestors may obtain additional copies from the Defense Documentation Center. All others should apply to the National Technical Information Service.

Unclassified

SECURITY CLASSIFICATION OF THIS PAGE (When Data Entered)

REPORT DOCUMENTATION PAGE		READ INSTRUCTIONS BEFORE COMPLETING FORM
1. REPORT NUMBER AFCRL-TR-75-0231	2. GOVT ACCESSION NO.	3. RECIPIENT'S CATALOG NUMBER
4. TITLE (and Subtitle) EFFECTS OF AIRPLANE FLOWFIELDS ON CLOUD WATER CONTENT MEASUREMENTS		5. TYPE OF REPORT & PERIOD COVERED Final Report 19 Sept. 74 - 30 Apr. 75
		6. PERFORMING ORG. REPORT NUMBER
7. AUTHOR(s) Hillyer G. Norment		8. CONTRACT OR GRANT NUMBER(s) F19628-75-C-0053
9. PERFORMING ORGANIZATION NAME AND ADDRESS Mt. Auburn Research Associates, Inc. 381 Elliot Street Newton, Massachusetts 02164		10. PROGRAM ELEMENT, PROJECT, TASK AREA & WORK UNIT NUMBERS 7605-04-01 63311F
11. CONTROLLING OFFICE NAME AND ADDRESS Air Force Cambridge Research Laboratories (LYC) Hanscom AFB, Massachusetts 01731 Contract Monitor: Mr. Morton Glass		12. REPORT DATE 30 April 1975
		13. NUMBER OF PAGES 79
14. MONITORING AGENCY NAME & ADDRESS (if different from Controlling Office)		15. SECURITY CLASS. (of this report) Unclassified
		15a. DECLASSIFICATION/DOWNGRADING SCHEDULE

16. DISTRIBUTION STATEMENT (of this Report)

Approved for public release; distribution unlimited.

17. DISTRIBUTION STATEMENT (of the abstract entered in Block 20, if different from Report)

18. SUPPLEMENTARY NOTES

19. KEY WORDS (Continue on reverse side if necessary and identify by block number)

cloud physics
hydrometeor concentration
water content
Lockheed C130A, C130E
concentration factor
meteorological research airplanes
effect of airflow on particle concentration
calibration of airborne hydrometeor samplers
AFCRL/SAMS Rain Erosion Program

20. ABSTRACT (Continue on reverse side if necessary and identify by block number)

Hydrometeor concentrations seen by fuselage-mounted particle measurement instruments are distorted owing to flow around the airplane. A general, three-dimensional method is used to compute flow-caused concentration distortion for specific sampling sites on two C130 cloud physics research airplanes. Results are presented for a variety of hydrometeor types (rain, snow and ice) over broad ranges of particle size.

DD FORM 1 JAN 73 1473 EDITION OF 1 NOV 65 IS OBSOLETE

Unclassified

SECURITY CLASSIFICATION OF THIS PAGE (When Data Entered)

The distortion results are combined with vertical profiles of water content, size spectra and hydrometeor type in nimbostratus clouds derived from radar data by the AFCRL/SAMS Rain Erosion Program. Integration of the resulting distorted water contents over missile trajectories through the clouds indicate that substantial errors in cumulative water contents are expected when hydrometeor concentrations are obtained by instruments mounted on airplane fuselages.

Flow-caused concentration distortion at wing-mounted instruments is studied qualitatively. Insignificant distortion is indicated.

Computational results are presented which indicate that deviations from free-fall orientation of ice crystals as they pass fuselage-mounted linear optical array particle spectrometers can very substantially bias size measurements of large crystals.

PREFACE

The author acknowledges with gratitude the support and guidance of Arnold Barnes, Morton Glass, Vernon Plank, and Robert Cunningham of the Meteorology Laboratory, AFCRL.

The project was supported by AFCRL as part of the Advanced Ballistics Reentry Systems (ABRES) program.

TABLE OF CONTENTS

LIST OF FIGURES

LIST OF FIGURES (continued)

LIST OF FIGURES (continued)

LIST OF TABLES

INTRODUCTION

Hydrometeor concentrations aloft are determined by radar and by airplane-mounted samplers. Radar measurements are strongly biased toward the larger particle sizes, and do not discriminate between hydrometeor types. Airplane samples can be used to calibrate the radar measurements, identify hydrometeor types, and fill out the small-particle tails of the size distributions.

There are several difficulties with the airplane sampling techniques. Among these are: restricted spatial and temporal range, small sampling volume, and concentration distortion caused by airflow around the airplane. In this report we consider only the last of these difficulties.

In Ref. 1 we describe a general, three-dimensional method by which flow-caused concentration distortion can be calculated. The method accounts for details of fuselage shape, airspeed, angle-of-attack, and altitude. It was applied to specific fuselage sampling sites on three research airplanes. Results at these sites are reported for water drops and ice columns over broad ranges of particle size.

In this report we extend our capability to treat ice plates, plane dendrites, and crystal aggregates. This allows illustrative calculations to be made of the way flow distortion errors in hydrometeor concentration measurements affect calculated water content along missile trajectories through nimbostratus clouds. For this purpose we use AFCRL/SAMS Rain Erosion Program water content and size spectra data published

---

1. H. G. Norment and R. G. Zalosh, "Effects of Airplane Flow Fields On Hydrometeor Concentration Measurements," Mt. Auburn Research Associates, AFCRL-TR-74-0602 (6 December 1974).

by Plank[2,3,4]. The calculations are performed for the site of a formvar particle replicator mounted on the fuselage of the AFCRL C130E cloud physics research airplane.

In Appendix A we examine the effect of airflow hydrometeor concentration measurements made by particle spectrometers mounted on converted fuel tank pods that are slung beneath the wings of the C130 airplanes. A semi-quantitative analysis indicates negligable flow effects.

Finally in Appendix B we investigate possible consequences on hydrometeor size measurements of flow-caused preferred orientation of ice crystals as they pass through linear-array optical spectrometers.

---

2. V. G. Plank, "Hydrometeor Parameters Determined From the Radar Data of the SAMS Rain Erosion Program. AFCRL/SAMS Report No. 2," AFCRL-TR-74-0249, Environmental Research Papers, No. 477 (4 June 1974).

3. V. G. Plank, "Liquid-Water-Content and Hydrometeor Size-Distribution Information for the SAMS Missile Flights of the 1971-72 Season at Wallops Island, Virginia. AFCRL/SAMS Report No. 3," AFCRL-TR-74-0296, Special Reports, No. 178 (2 July 1974).

4. V. G. Plank, "Liquid-Water-Content and Hydrometeor Size-Distribution Information for the SAMS Missile Flights of the 1972-73 Season at Wallops Island, Virginia. AFCRL/SAMS Report No. 4," in preparation.

BACKGROUND*

NATURE OF THE PROBLEM

Particle sampling devices of interest here measure particle flux through a small space adjacent to an airplane fuselage. Unless the sampling space is distant enough from the airplane to be in the free-stream, particles of certain sizes will interact with the curvilinear flow about the fuselage to cause flux distortion. The situation is illustrated in Fig. 1 for 100 μm diameter water drops in airflow about a prolate ellipsoid of fineness ratio 2. Note the impaction on the ellipsoid of the drop closest to the ellipsoid symmetry axis, and note the substantial deflections of the next closest trajectories. Drop deflection causes high particle concentrations and concentration gradients to be observed at a point such as the one marked X 1 in the figure. At point X 2, defliction and impaction combine to produce a region void of particles, a so-called "shadow zone". Smaller drops, with much less inertia, tend to follow the airflow more exactly such that lesser distortion is observed. Drops large enough to have very high inertia substantially ignore the airflow, and again little distortion is observed. Therefore, for water drops, and ice crystals as well, distortion is significant over a limited, intermediate range of particle sizes.

CONCENTRATION FACTOR

Principal results of this work are expressed in a quantity called concentration factor. Concentration factor, C_F, is defined as the ratio of particle flux (i.e., mass of particles passing per second

---

* This chapter is a synopsis of information given in Ref. 1. The reader is referred to that report for details.

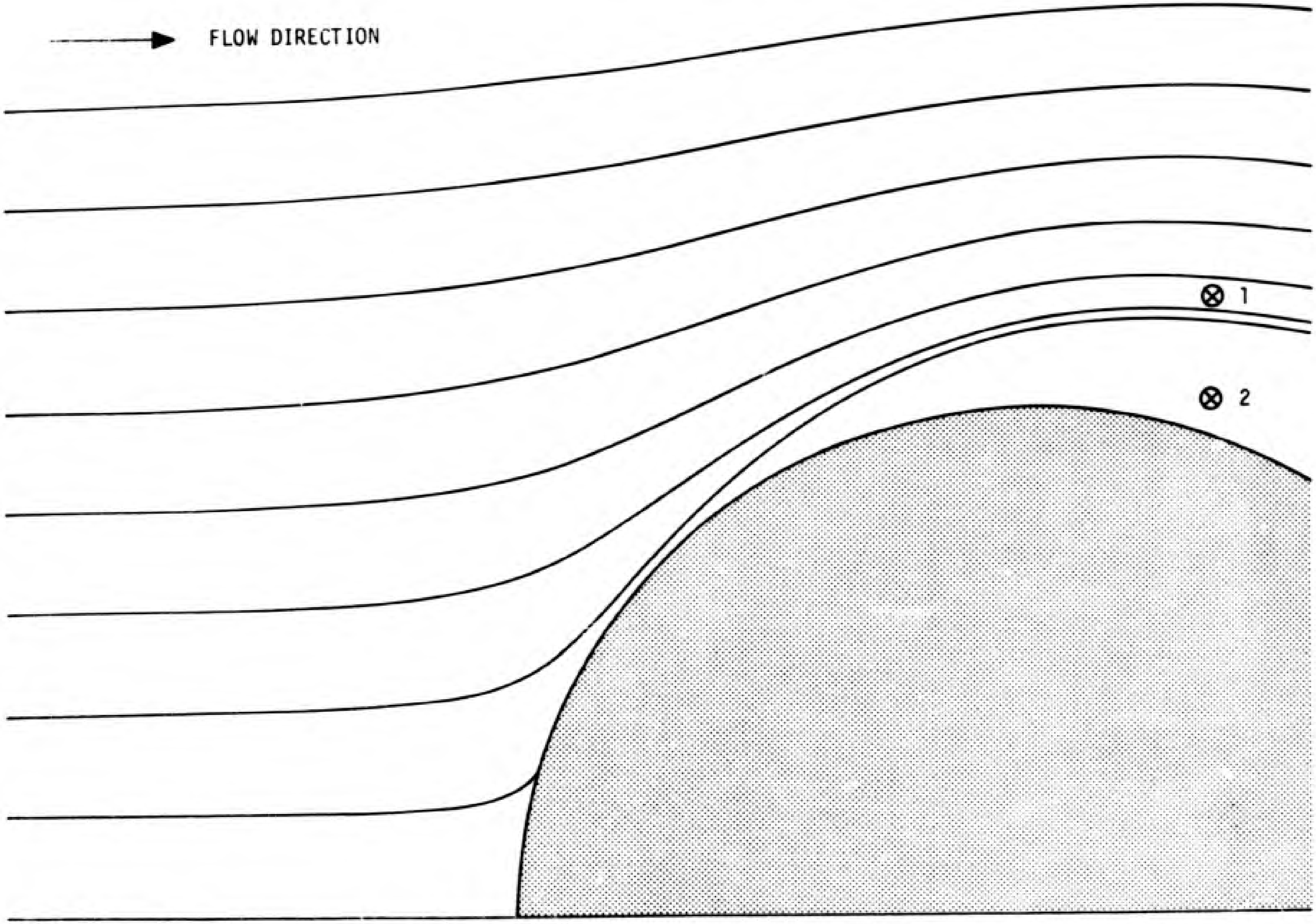

FIGURE 1. Trajectories of 100 μm diameter water drops in potential airflow about a prolate ellipsoid of fineness ratio 2. (The ordinate scale is expanded by a factor of 2.)

through a unit area normal to the particle velocity) at the sampling or target point, F_t, to the particle flux in the free-stream, F,

$$C_F \equiv \frac{F_t}{F} \quad . \tag{1}$$

The ratio of particle concentration at the target point to free-stream concentration, C_M, is

$$C_M = C_F \, V/V_t, \tag{2}$$

where V is free-stream airspeed and V_t is airspeed at the target point. In this latter definition we ignore difference between particle and air velocities.

In three dimensions we determine concentration factor via calculation of a particle flux tube (Fig. 2). This tube, which is analogous to a streamtube, is determined such that there is no particle flux through its boundaries; therefore mass transfer rate of particles is equal through all cross-sections. The tube is centered about a trajectory (the heavy dashed curve in Fig. 2) that passes through the primary target point. The initial and target planes are perpendicular to the central trajectory.

If m is the particle mass transfer rate through the tube, then at any point along the tube

$$\dot{m} = FA, \tag{3}$$

where A is the perpendicular cross section area of the tube. Since $\dot{m}$ is constant in a particle flux tube,

$$C_F = \frac{A}{A_t} \quad , \tag{4}$$

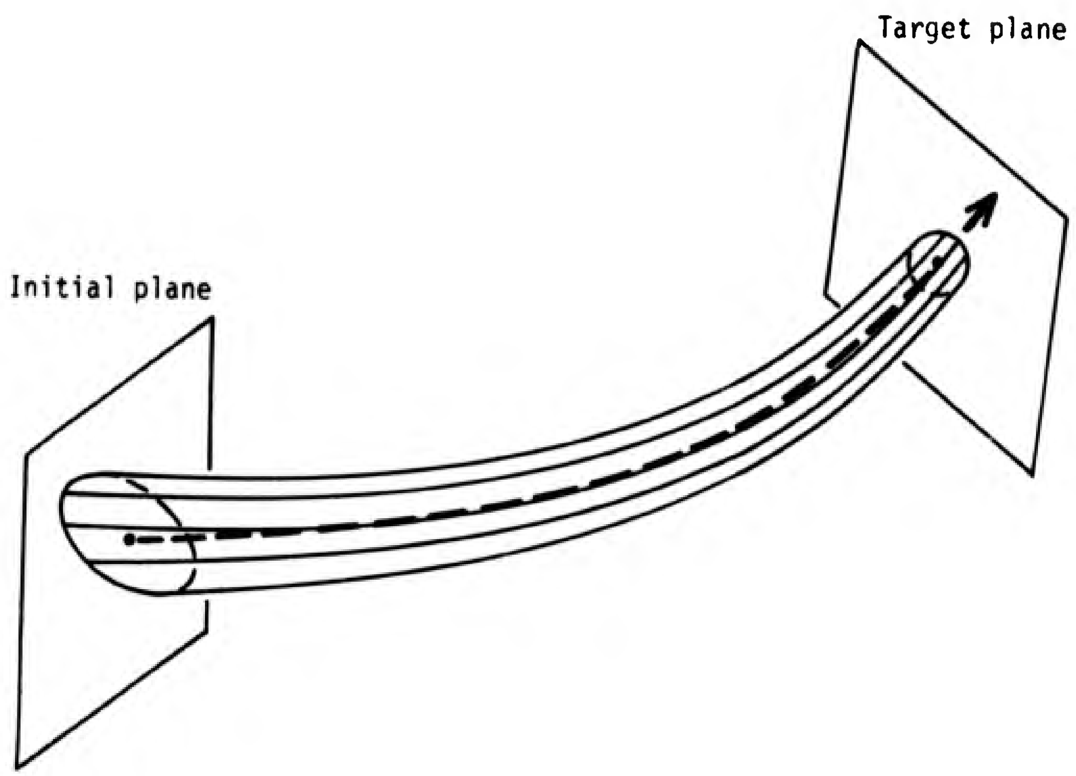

FIGURE 2. Perspective view of a particle flux tube.

or

$$C_F = \lim_{\substack{A \to 0 \\ A_t \to 0}} \left(\frac{A}{A_t}\right) \quad , \tag{5}$$

where A and A_t are the cross-sectional areas of the flux tube in the free-stream and at the target point, respectively.

In broad outline, our procedure is as follows. We define a circular "window" (i.e. flux tube surface trace) in the target plane. Our primary target point is at the center of this circle. A number of evenly spaced points (usually 6 or 8) are chosen on the window circumference. Then, by use of an iterative procedure, described in Ref. 1, we establish the particle trajectories that pass through these points. We take the trajectory intersection points with the target and initial planes to be the vertices of plane polygons: an approximate regular polygon in the target plane, and an irregular (distorted) polygon in the initial plane. We compute the areas of these polygons, and take the concentration factor to be the ratio of these areas.

PARTICLE TRAJECTORY CALCULATION

The equations of motion of a heavy particle in a fluid are based on the assumption that the bulk fluid flow is not perturbed by the particles. Therefore, the particles move under influence of the forces of aerodynamic drag, gravity, buoyancy, and inertial reaction of fluid carried along. For particles small enough for application of Stokes drag law, the theory is quite adequately developed. For large particles, the theory is deficient and we must resort to use of approximations to the aerodynamic drag during accelerative motion.

If the particle density is large compared to the fluid, which is true for hydrometeors in air, we can neglect buoyancy and inertial reaction of the fluid to obtain the general equation

$$m \frac{d\vec{V}_p}{dt} = \frac{1}{2} \rho A_p (\vec{V}_f - \vec{V}_p) \left|\vec{V}_f - \vec{V}_p\right| C_D + m\vec{g} \tag{6}$$

where m is the particle mass, A_p the particle area projected in the direction of motion, $\vec{V}_p$ particle velocity, $\vec{V}_f$ fluid velocity, C_D drag coeffieicnt, ρ fluid density, and $\vec{g}$ gravity acceleration. Consider a flow of constant free-stream airspeed V around a body of characteristic dimension L.* Then Eq. (6) can be non-dimensionalized to yield

$$\frac{dv_{px}}{d\tau} = (v_{fx} - v_{px}) \frac{P}{P_T v_T F_N}$$

$$\frac{dv_{py}}{d\tau} = (v_{fy} - v_{py}) \frac{P}{P_T v_T F_N}$$

$$\frac{dv_{pz}}{d\tau} = (v_{fz} - v_{pz}) \frac{P}{P_T v_T F_N} - \frac{1}{F_N} \quad . \tag{7}$$

Here length is scaled by L, velocity by V, time by L/V, and

$$P = \left(C_D R_N^2\right) / R_N \tag{8}$$

$$F_N = V^2/(Lg) \tag{9}$$

$$R_N = \frac{\rho\delta}{\eta} \left| \vec{v}_p - \vec{v}_f \right| V \quad . \tag{10}$$

Non-dimensional quantities are:

$\vec{v}_p$, $\vec{v}_f$	particle and air velocities
τ	time

---

* Equivalent results are obtained by assuming either a moving body in a stationary fluid, or a moving fluid about a stationary body. Therefore we use whichever concept is most expedient.

F_N — Froude number

R_N — Reynolds number

$C_D R_N^2 = B_N$ — Best number

C_D — drag coefficient

v_T — terminal settling speed (P_T is computed from v_T)

Dimensioned quantities are:

δ — particle dimension

ρ — air density

η — air viscosity

g — gravity acceleration constant

V — free-stream airspeed

L — characteristic dimension of body

In this form, the equations are applicable to any flow and to any size and shape of particle.

For Stokes drag ($R_N < 0.1$) P has the constant value 24. For larger R_N, P is a function of Reynolds number and acceleration; however the dependence on acceleration is not known. It is customary practice to use steady-state values of P, which are determined from terminal settling experiments. Use of these data are discussed in Ref. 1.

Equations (7) are integrated numerically starting at a point far enough upstream that essentially free-stream conditions prevail. Krogh's ordinary differential equation integrator DVDQ(5) is used. The technique used to compute $\vec{v}_f$ at each time step is described next.

---

5. F. T. Krogh, "Variable Order Integrators for Numerical Solution of Ordinary Differential Equations," Jet Propulsion Lab Technology Utilization Document No. CP-2308 (November 1970).

THREE-DIMENSIONAL FLOW CALCULATION

In performing concentration factor calculations for sampling sites on particular airplanes, it is important to use three-dimensional airflow. This is the only way to adequately account for particle settling, airplane geometry, angle-of-attack, airspeed and altitude.

Cloud physics airplanes are subsonic, sampling runs being made typically between 100-150 kts. indicated airspeed. Particle measurement points are beyond the skin-friction boundary layer, and should be placed to avoid separated flow regions. Therefore, potential (i.e., frictionless, incompressible, laminar) flow calculations are quite adequate. We use a code developed by Hess and Smith(6,7) for calculating potential flow about arbitrary three-dimensional bodies. (Recent, more generalized methods reduce to the Hess-Smith procedure for comparable application(8).) The Hess-Smith code requires input of a digital description of the aircraft surface. This consists of the coordinates of the corner points of a large number of contiguous, plane, quadralaterals. An example of the digital description of a fuselage is shown in Figs. 3 and 4.

---

6. J. L. Hess and A. M. O. Smith, "Calculation of Non-Lifting Potential Flow About Arbitrary Three-Dimensional Bodies," McDonnell Douglas Report E. S. 40622 (15 March 1962). AD-282 255.

7. J. L. Hess and A. M. O. Smith, "Calculation of Potential Flow About Arbitrary Bodies," in Progress in Aeronautical Sciences, Vol. 8, edited by D. Kuchemann (Pergamon Press, New York, 1967).

8. F. A. Woodward, "Analysis and Design of Wind-Body Combinations at Subsonic and Supersonic Speeds," J. Aircraft 5, 528 (1968).

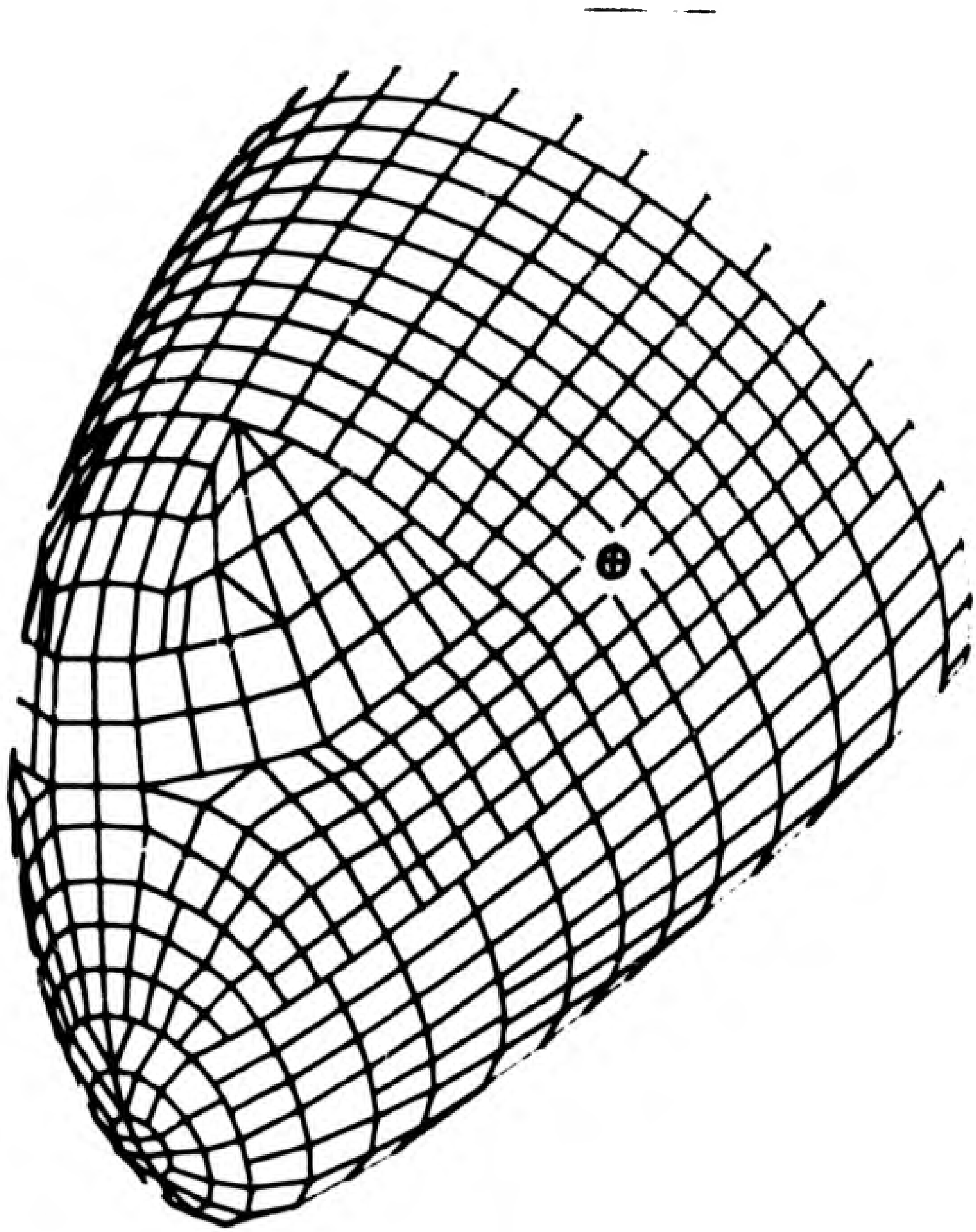

FIGURE 3. Computer-prepared plot of the digital description of the nose and cabin sections of the Lockheed C130A airplane. ⊗ marks the location of the formvar replicator.

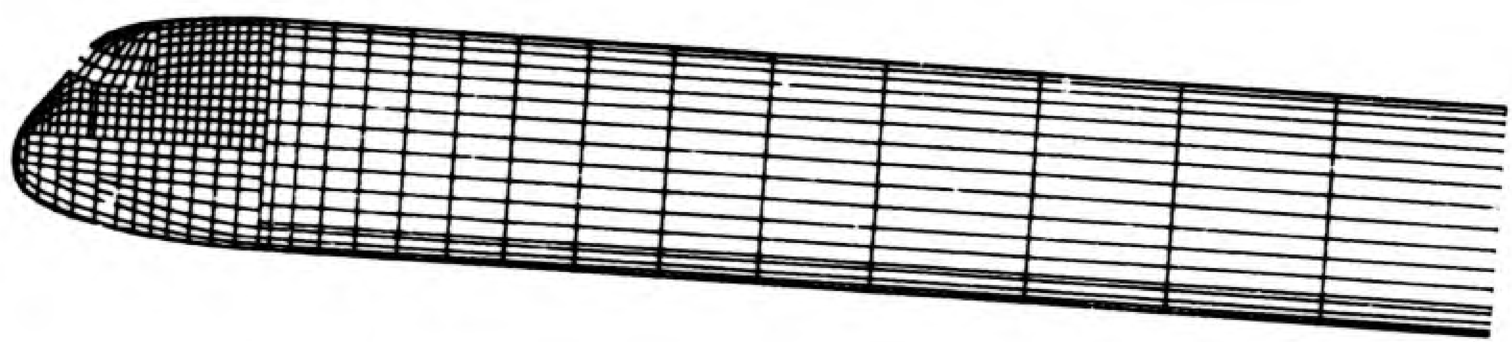

FIGURE 4. Computer-prepared plot of the digital description of the complete Lockheed C130A fuselage. The upward tilt of the nose represents a 4° angle-of-attack.

SAMPLING SITES STUDIED

FORMVAR REPLICATOR ON THE LOCKHEED C130A

The Lockheed C130A transport, outfitted for cloud physics studies by the Convective Cloud Physics Branch, Air Force Cambridge Research Laboratories, is shown in Fig. 5. We have performed extensive concentration factor calculations at the site of the intake slit of a formvar replicator (Fig. 6). The replicator arm exits the fuselage at the point marked X in Fig. 3. It is mounted perpendicular to the fuselage symmetry plane. The intake slit is 14.3 inches from the fuselage, measured along the arm. Flight conditions and relative airspeed at the replicator slit are given in Table 1. Details concerning the replicator location are given in Ref. 1.

FORMVAR REPLICATOR ON THE LOCKHEED C130E

With respect to its external shape, the Lockheed C130E fuselage is identical with that of the C130A except for the nose radome. The difference is obvious by comparison of Figs. 3 and 4 with Fig. 7. Concentration factor results presented in Ref. 1 suggest that a formvar replicator with arm length similar to the one mounted on the C130A would lie in a "shadowed zone" for water drops over a consider range of sizes. Consequently, replicator arm length has been extended 8 inches. Its point of exit from the fuselage is the same as before (Fig. 7). Its geometry in a plane perpendicular to the fuselage axis is shown in Fig. 8. Concentration factor calculations reported here are for the site of the intake slit on this modified replicator. Flight conditions and relative airspeed at the replicator slit are given in Table 1.

---

9. J. Hallett, R. W. Hanaway, and P. B. Wagner, "Design and Construction of a New Cloud Particle Replicator for Use on a Pressurized Aircraft," Desert Research Institute, Reno, Nevada, AFCRL-72-0410 (31 May 1972). AD-753 091.

FIGURE 5. Lockheed C130A transport outfitted for cloud physics studies. Wingspan - 132 feet; overall length - 95 feet; fuselage radius $\sim$ 85 inches. Locations of the particle replicators are shown in Figs. 3 and 7.

FIGURE 6. Lockheed C130A with formvar replicator arm in position (flowplate not mounted).

TABLE 1

A. FLIGHT CONDITIONS

Altitude (kft)	Indicated Air-speed (kts)	True Air-speed (kts)	Angle-of-Attack (deg)	Temperature (^oK)	Air Density (kg/m^3)	Air Viscosity (kg/(m-sec))
5	162	177.6	4^o	278.3	1.055	1.741×10^{-5}
30	162	265.1	4^o	229.5	0.459	1.491×10^{-5}

B. AIRSPEED RELATIVE TO FREE-STREAM AT SAMPLING POINTS

Airplane	Instrument	v_t
Lockheed C130A	Formvar Replicator	1.10
Lockheed C130E	Formvar Replicator	1.04

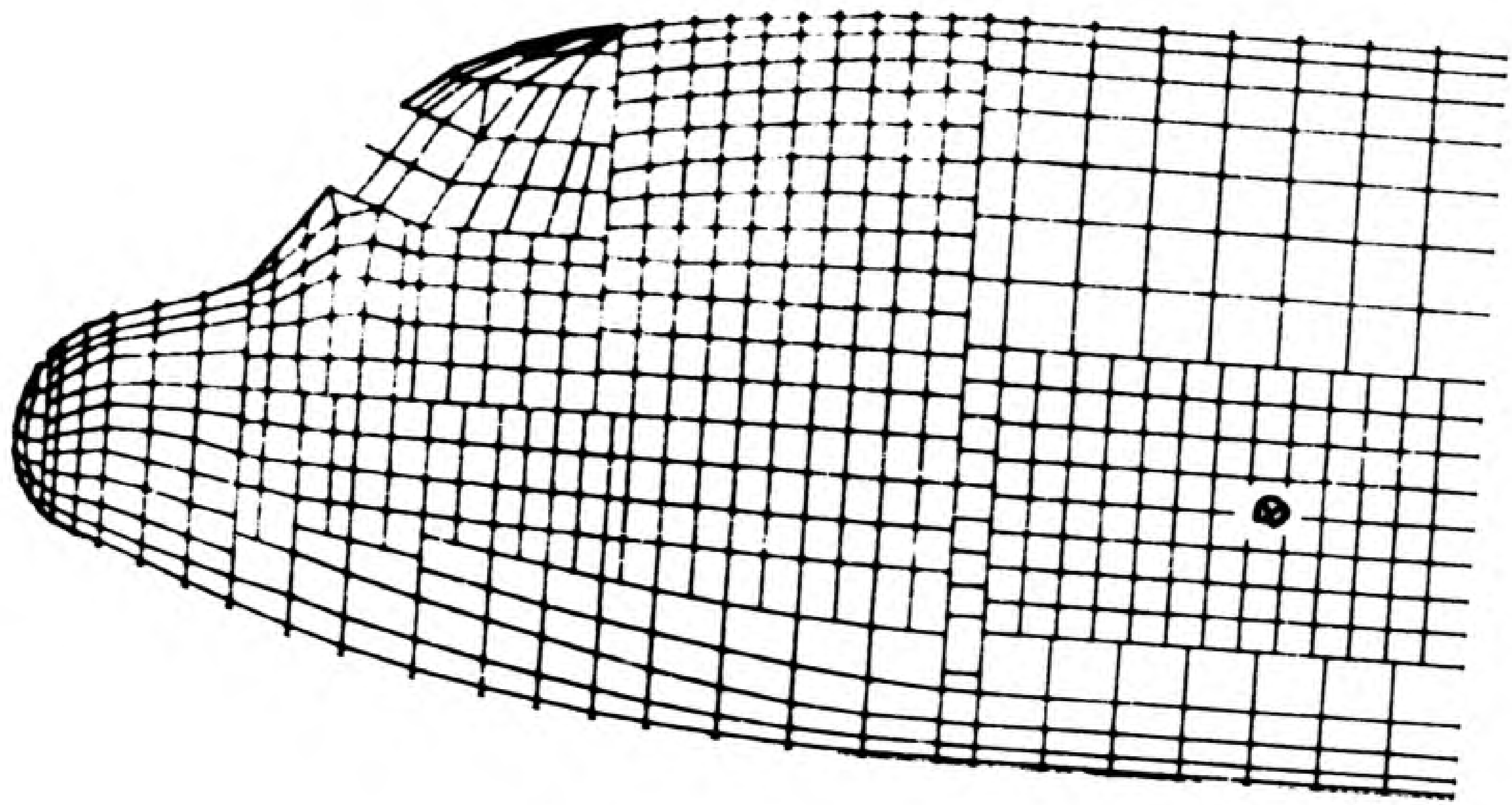

FIGURE 7. Computer-prepared plot of the digital description of the Lockheed C130E forward fuselage to FS 350". ⊗ marks the location of the formvar replicator.

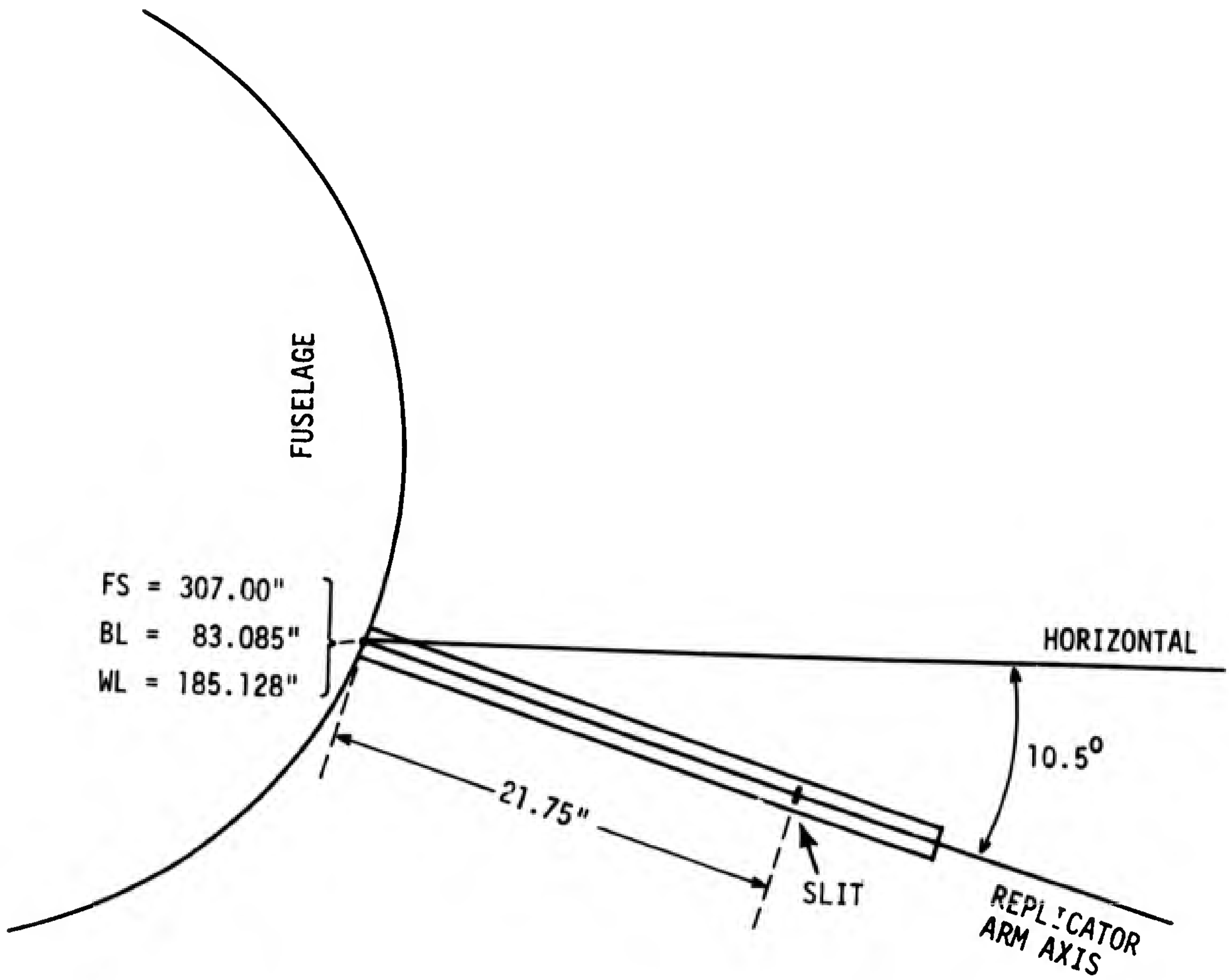

FIGURE 8. Formvar replicator arm geometry on the Lockheed C130E. (Not drawn to scale.)

HYDROMETEOR TYPES AND CONCENTRATION FACTOR RESULTS

Solution of Eqs. (7) for particles in flow around a solid body requires that the aerodynamic drag coefficient or Best number, B_N, be known as a function of Reynolds number, R_N, for relative velocity of particle and air. It also requires that Reynolds number for terminal settling be known as a function of Best number. The R_N - B_N relationships for terminal settling are accurately known for a variety of particle shapes. The B_N - R_N relations required to solve Eqs. (7) for accelerative motion are developed from the steady, terminal settling data as discussed in Ref. 1 for water drops and ice columns. Here we present additional C_F results for water drops and ice columns, and extend our capabilities and results to additional ice crystal and crystal aggregate forms.

WATER DROPS AND ICE COLUMNS

Concentration factor results for water drops at the C130A replicator slit at 5 and 30 kft are presented in Ref. 1. Similar results at the modified C130E replicator slit are shown here in Fig. 9 and listed in Table 2.

In Ref. 1 results for solid and hollow ice columns at the C130A replicator slit at 5 kft are presented. Properties of columnar ice crystals, determined as described in Ref. 1, are presented here in Table 3 in terms of dimensions and other properties shown in Fig. 10. The quantity $< \nabla >$ is the mean dimension of a column that assumes random orientation in a plane parallel with its long axis, as seen projected in a direction parallel with the plane. It is given by (see Appendix C of Ref. 1 and Appendix B below).

$$< \nabla > = \frac{2}{\pi} (\delta + \ell) \quad . \tag{11}$$

Concentration factor results at the modified C130E replicator

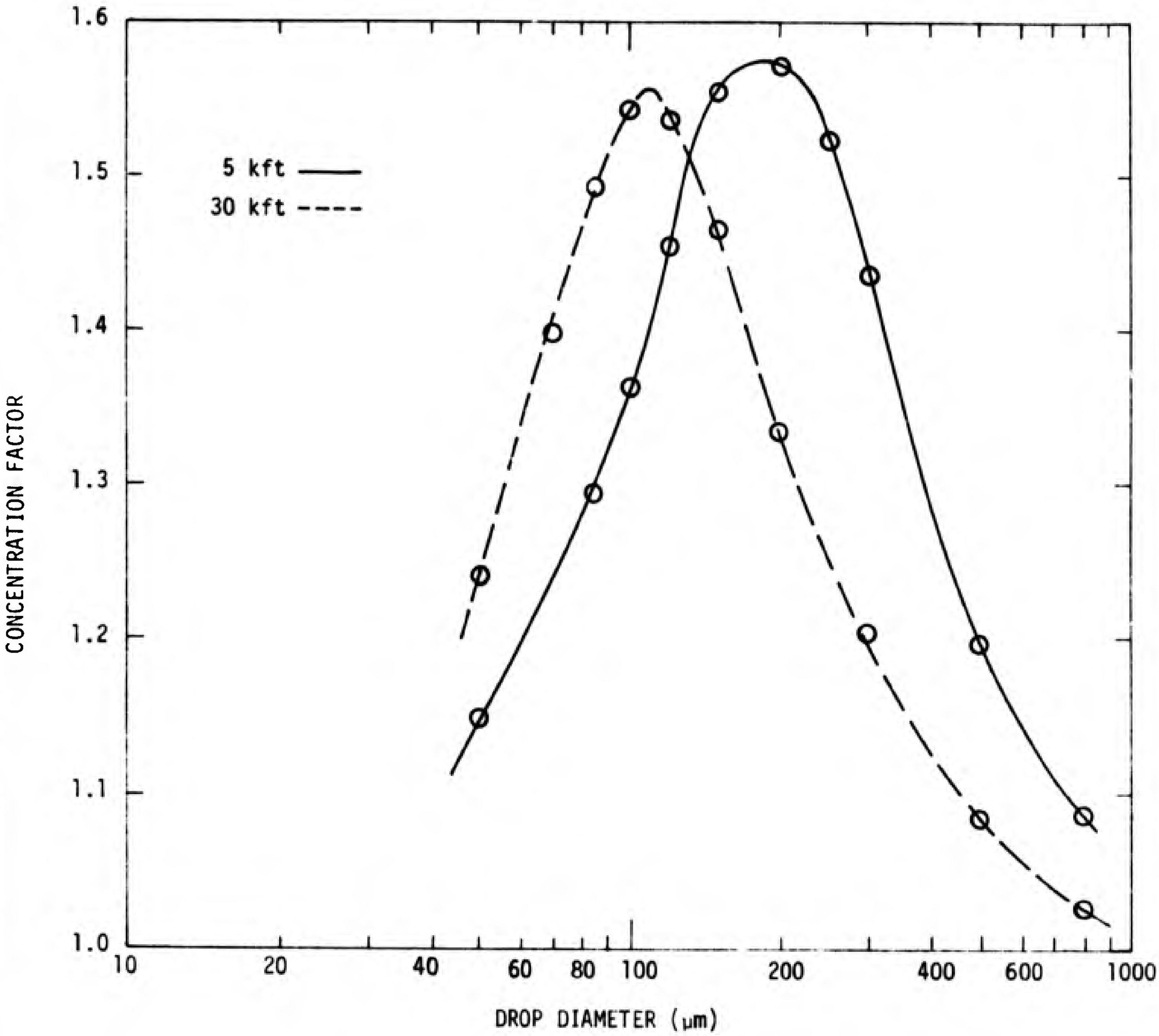

FIGURE 9. Concentration factors vs water drop diameter at the Lockheed C130E formvar replicator slit.

TABLE 2

WATER DROP CONCENTRATION FACTORS AT THE LOCKHEED C130E FORMVAR REPLICATOR SLIT

Drop Diameter (μm)	Drop Mass (μg)	Concentration Factors	
		5 kft Altitude	30 kft Altitude
50	.0655	1.149	1.241
70	.1796		1.400
85	.3216	1.296	1.494
100	.524	1.365	1.545
120	.905	1.454	1.538
150	1.767	1.558	1.467
200	4.189	1.573	1.336
250	8.18	1.524	
300	14.14	1.436	1.205
500	65.45	1.199	1.084
800	268.1	1.088	1.027

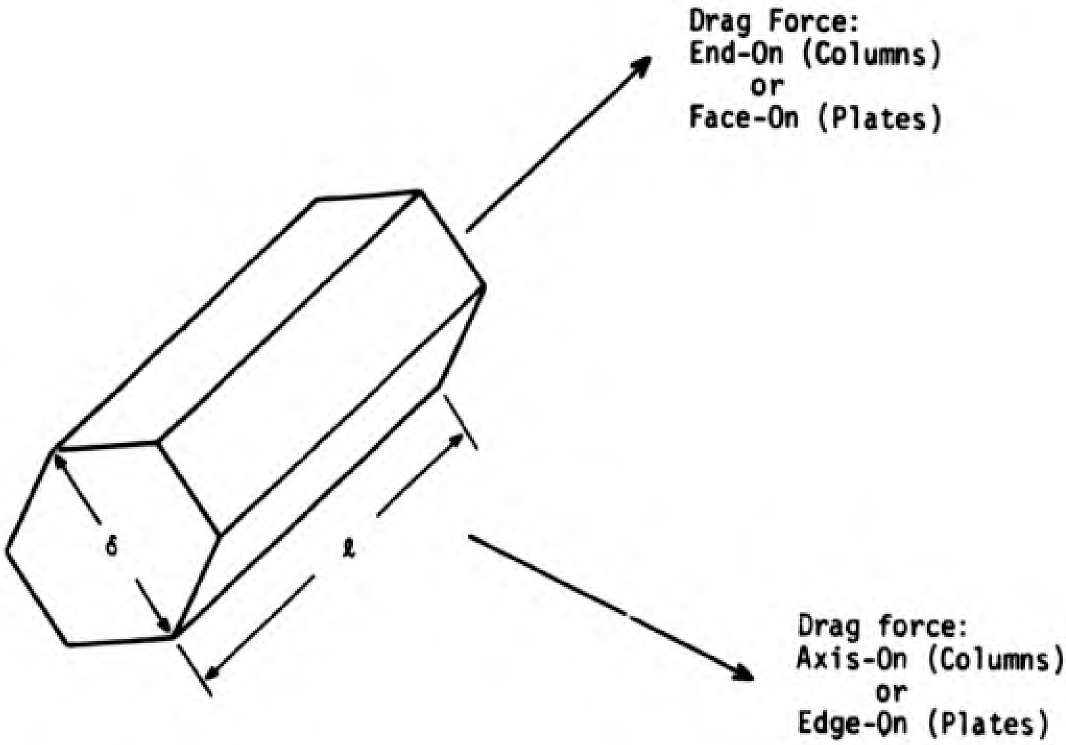

Volume:

$$Vol = \frac{3\sqrt{3}}{8}\ \delta^2\ell = 0.649519\delta^2\ell$$

Mass:

$$m = 0.649519\delta^2\ell\ \rho_p$$

Diameter of Water Drop of Equal Mass:

$$\delta_w = 1.0744786(\delta^2\ell\ \rho_p/\rho_{water})$$

FIGURE 10. Properties of hexagonal-based plates and columns.

TABLE 3

PROPERTIES OF COLUMNAR ICE CRYSTALS

				Solid Columns*		Hollow Columns*	
Length, ℓ (μm)	Width, δ (μm)	δ/ℓ	$<\nabla>$	Mass (μg)	Diameter of water drop of equal mass (μm)	Mass (μg)	Diameter of water drop of equal mass (μm)
50	35.8	.715	54.62	.0291	38.1	.0149	30.6
70	50.2	.717	76.52	.0802	53.5	.0412	42.9
85	59.8	.703	92.18	.138	64.1	.0710	51.4
100	68.3	.683	107.14	.212	74.0	.1091	59.3
190	93.4	.492	180.32	.753	112.9	.387	90.4
300	117.0	.390	265.47	1.87	152.8	.960	122.4
500	144.5	.289	410.30	4.75	208.5	2.441	167.1
700	165.9	.237	551.25	8.76	255.8	4.505	204.9
900	183.6	.204	689.8	13.8	297.6	7.094	238.4
1000	197.3	.197	762.2	17.7	323.3	9.100	259.0
1500	226.5	.151	1099.1	35.0	405.8	17.99	325.1
2000	262.8	.131	1440.5	62.8	493.3	32.32	395.2
3000	310.9	.104	2107.8	131.9	631.5	67.82	506.0
4000	350.2	.088	2769.4	223.1	752.4	114.72	602.8

* Solid column density is taken to be 0.7 g/cm^3, and hollow column density is taken to be 0.36 g/cm^3.

slit at 5 and 30 kft for solid and hollow columns are given in Fig. 11, and Table 4. These results are for the "axis-on" orientation (Fig. 10).

HEXAGONAL PLATES (Pla)*

Free-fall settling properties of discs, which have settling properties essentially the same as hexagonal plates, have been studied by a number of workers. They all agree that in the viscous flow range (R_N<1) discs show no preferred orientation of fall. Wadell[10] reports that preferred orientation begins at about $R_N = 0.5$. Jayaweera and Mason[11] claim that ".... all discs with R_N>0.07 fall with their short axes vertical and present maximum resistance to motion." Kajikawa[12] states that for ℓ/δ (thickness/diameter) = 0.1, the edge-on orientation of fall (see Fig. 10) is stable only for $R_N \lesssim 0.15$.

Willmarth, Hawk and Harvey[13] discuss in detail the behavior of free-falling discs in the R_N interval from 1-100. Their study covers ℓ/δ values from .00167-.042. They find for R_N slightly greater than one that discs very rapidly orient to the face-on orientation. As R_N increases a tendency to oscillate about the equilibrium orientation increases. Willmarth, Hawk and Harvey report that the oscillations become unstable in the range $100 \lesssim R_N \lesssim 170$. However, List and

---

* The crystal type notation of Magano and Lee (J. Fac. of Sci., Hokkaido U., Ser. VII, Vol. II, 321 (1966)) is used.

10. H. Wadell, "The Coefficient of Resistance as a Function of Reynolds Number for Solids of Various Shapes," J. Franklin Inst. 217, 459 (1937).

11. K. O. L. F. Jayaweera and B. J. Mason, "The Falling Motions of Loaded Cylinders and Discs Simulating Snow Crystals," Quart. J. Roy. Meteor. Soc. 92, 151 (1966).

12. M. Kajikawa, "A Model Experimental Study on the Falling Velocity of Ice Crystals," J. Meteor. Soc. Japan 49, 367 (1971).

13. W. W. Willmarth, N. E. Hawk, and R. L. Harvey, "Steady and Unsteady Motions and Wakes of Freely Falling Disks," The Physics of Fluids 7, 197 (1964).

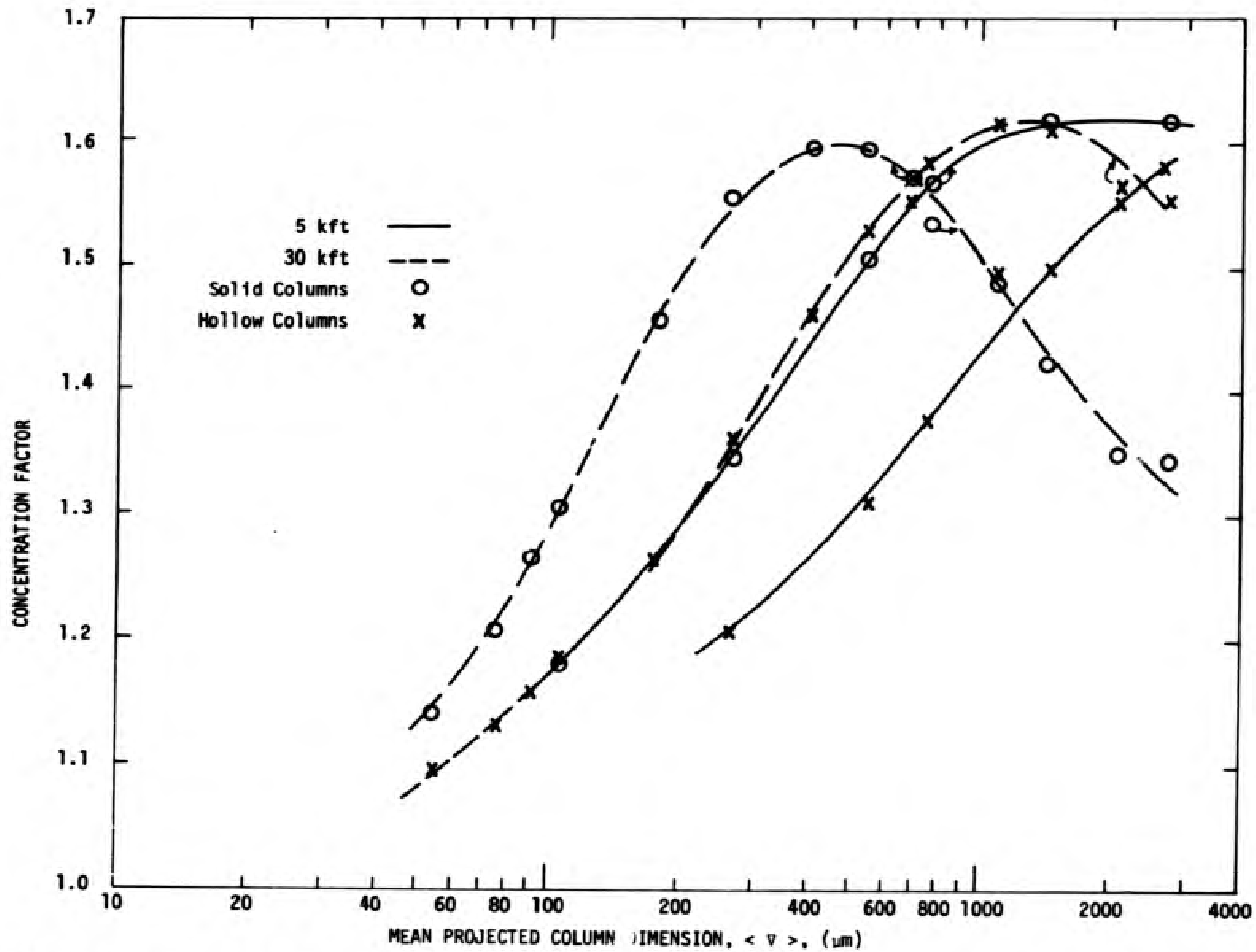

FIGURE 11. Concentration factor vs. ice column mean projected dimension at the Lockheed C130E formvar replicator slit.

TABLE 4

ICE COLUMN CONCENTRATION FACTORS AT THE LOCKHEED C130E FORMVAR REPLICATOR SLIT

Length	Width	< ∇ >	Solid Columns		Hollow Columns	
(μm)	(μm)	(μm)	5 kft	30 kft	5 kft	30 kft
50	35.8	54.6		1.139		1.097
70	50.2	76.5		1.207		1.130
85	59.8	92.2		1.264		1.159
100	68.3	107.1	1.183	1.303		1.186
190	93.4	180.		1.455		1.270
300	117.0	265.	1.347	1.553	1.208	1.362
500	144.5	410.		1.593		1.460
700	165.9	551.	1.506	1.593	1.310	1.529
900	183.6	690.		1.570		1.557
1000	197.3	762.	1.569	1.534	1.375	1.582
1500	226.5	1099.		1.483	1.446	1.615
2000	262.8	1440.	1.616	1.420	1.498	1.610
3000	310.9	2108.		1.348	1.555	1.564
4000	350.2	2769.	1.618	1.342	1.582	1.554

Schemenauer(14), who studied six symmetrical plane ice crystal models ranging from a solid circular disc to a stellar shape, found that " ... no oscillations were observed for $R_N \leq 100$. By $R_N \approx 200$ small oscillations were only observed in the disc, hexagonal plate and broad-branched crystal models, the oscillations being the greatest in the case of the disc."

Computed Reynolds numbers for hexagonal plates over a range of sizes at the C130A and C130E replicator intake slits at 30 kft altitude are shown in Table 5. Only for the largest plates is there much likelihood of instability. Therefore, we can assume that the plates are stably oriented with their plane faces perpendicular to the drag force vector. The direction of the drag force vector is discussed below in Appendix B.

Graphs of R_N (Reynolds number) vs. B_N (Best number) for plates of various ℓ/δ values are given by Jayaweera and Cottis(15), List and Schemenauer(14) and Kajikawa(12). Data are tabulated by Will-Willmarth, Hawk and Harvey(13). The graphical data were transferred from the published papers to lined graph paper as described on p. 87 of Ref. 1. For $R_N > 1$, the R_N vs. B_N relation is independent of ℓ/δ. The data from all of the sources were merged for $R_N > 1$ to determine polynomial relationships between R_N and B_N via least squares. For $R_N < 1$ ($B_{N,T} < 20$), the data of Kajikawa were merged with those of Jayaweera and Cottis to determine the R_N - B_N relationships for $\ell/\delta = 1.0$, 0.5, and 0.05.

---

14. R. List and R. S. Schemenauer, "Free-Fall Behavior of Planar Snow Crystals, Conical Graupel and Small Hail," J. Atmos. Sci. 28, 110 (1971).

15. K. O. L. F. Jayaweera and R. E. Cottis, "Fall Velocities of Plate-Like and Columnar Ice Crystals," Quart. J. Roy. Meteor. Soc. 95, 703 (1969).

TABLE 5

HEXAGONAL PLATE REYNOLDS NUMBERS AT THE FORMVAR REPLICATOR SLITS ON THE LOCKHEED C130A and C130E At 30 kft ALTITUDE

Plate Diameter (μm)	Reynolds Numbers C130A Replicator	C130E Replicator
50	4.5	1.0
100	11.8	3.3
200	34.5	12.0
300	69.2	27.3
400	113	48.1
500	163	74.2
600	214	109
800	331	197
1000	440	303

Polynomial coefficients are given in Table 6. Use of these polynomials is as described in Appendix B of Ref. 1. R_N and $B_{N,T}$ for circular discs are

$$R_N = \frac{\rho\delta}{\eta} |\vec{V}_p - \vec{V}_f| \tag{12}$$

$$B_{N,T} = \frac{2g\rho(\rho_p - \rho)}{\eta^2} \left(\frac{\ell}{\delta}\right) \delta^3 \quad , \tag{13}$$

where ρ and ρ_p are air and particle densities, η is air viscosity, $\vec{V}_p$ and $\vec{V}_f$ are particle and air velocities, g is the gravity acceleration constant, ℓ is disc thickness, δ is disc diameter,and $B_{N,T}$ is Best number for terminal gravity settling.

Kajikawa[16] has measured masses of various characteristic plane ice crystal forms. He has also measured δ vs. ℓ for these forms and his results agree well with those of Auer and Veal[17]. Here we combine the results of the mass measurements of Kajikawa with the dimensions of Auer and Veal. Properties of the hexagonal plate crystals are given in Table 7. The dimensional relation of Auer and Veal is

$$\ell = 2.020\ \delta^{0.449} \tag{14}$$

Concentration factor results for hexagonal plates at the Lockheed C130A and modified C130E formvar replicators are given in Fig. 12 and Table 8.

---

16. M. Kajikawa, "Measurement of Falling Velocity of Individual Snow Crystals," J. Meteor. Soc. Japan 50, 577 (1972).

17. A. H. Auer and D. L. Veal, "The Dimensions of Ice Crystals in Natural Clouds," J. Atmos. Sci. 27, 919 (1970).

TABLE 6

POLYNOMIAL COEFFICIENTS RELATING R_N and B_N FOR CIRCULAR DISCS

$$\log_{10} R_{N,T} = \sum_{j=0}^{2} b_j (\log_{10} B_{N,T})^j$$

ℓ/δ	b_0	b_1	b_2
($B_{N,T} \geq 20$)	-1.2556	1.0049	-0.050617
0.05	-1.1857	0.94093	-0.036059
0.5	-1.3100	1.0246	-0.052374
1.0	-1.3926	0.98869	-0.02163

$$\log_{10} B_N = \sum_{j=0}^{2} a_j (\log_{10} R_N)^j$$

ℓ/δ	a_0	a_1	a_2
($R_N \geq 1$)	1.3592	1.0811	0.13715
0.05	1.3263	1.2005	0.062923
0.5	1.3675	1.1642	0.091227
1.0	1.4513	1.0724	0.021773

TABLE 7

PROPERTIES OF HEXAGONAL PLATE (P1a) ICE CRYSTALS

Diameter (μm)	Thickness (μm)	Mass (μg)	Diameter of Water Drop of Equal Mass (μm)	Density (kg/m^3)
50	11.70	∿ 9.203×10^{-3}	∿ 26	∿ 484.0
100	15.97	∿ 3.351×10^{-2}	∿ 40	∿ 323.0
200	21.80	0.1575	67	278.0
300	26.16	0.4779	97	312.5
400	29.76	1.124	129	363.4
500	32.90	2.145	160	401.5
600	35.71	3.823	194	457.9
800	40.63	10.09	268	596.8
1000	44.91	20.22	338	693.1

TABLE 8

CONCENTRATION FACTORS AT THE LOCKHEED C130 FORMVAR REPLICATOR SLITS FOR HEXAGONAL PLATE ICE CRYSTALS (P1a)

Plate Diameter (μm)	Concentration Factors			
	C130A		C130E	
	5 kft	30 kft	5 kft	30 kft
50	1.146	1.180		1.080
100	1.165	1.202		1.095
200	1.205	1.267		1.130
300	1.248	1.344	1.119	1.187
400	1.299	1.408		1.244
500	1.344	1.440	1.175	1.295
600	1.384	1.457	1.209	1.368
800	1.453	1.440	1.298	1.515
1000	1.469	1.394	1.382	1.599

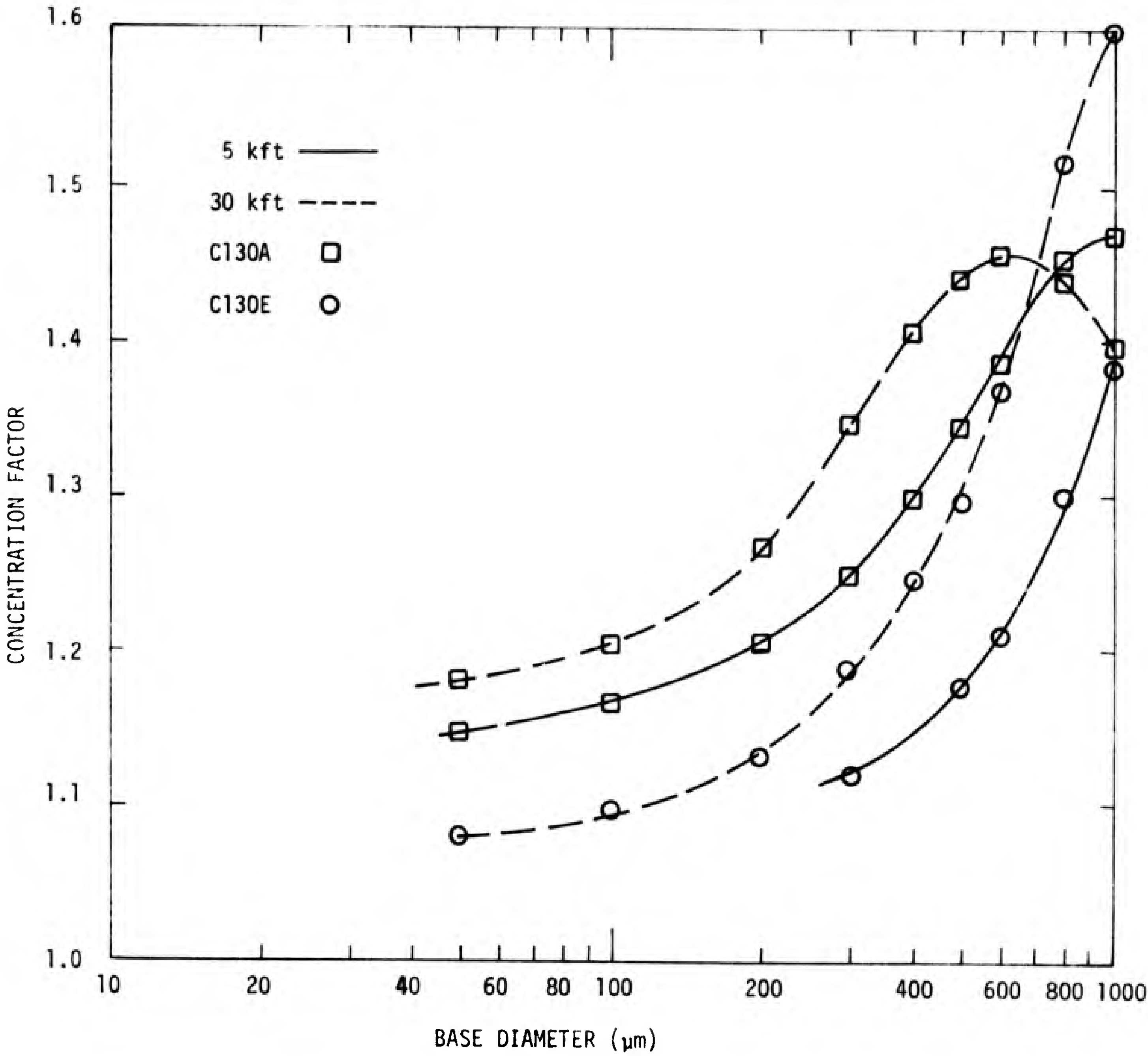

FIGURE 12. Concentration factor vs. hexagonal plate (Pla) base diameter at the Lockheed C130 formvar replicator slits.

PLANE DENDRITES (Ple)

Jayaweera[18] has found that circular disc drag data can be used for symmetrical plane ice crystals of virtually any form, with an error of not more than 25%, providing that the crystals are represented by discs of the same thickness and mass, i.e., equivalent discs. Shapes studied by Jayaweera are: circular disc, hexagonal plate (Pla), crystal with broad branches (Plc), stellar crystal (Pld), and a form intermediate between Plc and Pld.

As was done for the solid plates, we use data of Kajikawa and a fitted equation by Auer and Veal to obtain crystal mass, m, and thickness, ℓ, from specified diameter. To obtain the diameter of the equivalent disc, we use the Kajikawa-Auer and Veal data to construct a graph of density vs. mass for plate crystals (Pla). This was used to determine plate density, ρ_p, from the dendrite mass. The equivalent disc diameter was then approximated via the equation

$$\delta = \sqrt{\frac{8}{3\sqrt{3}} \frac{m}{\ell \rho_p}} \quad . \tag{15}$$

The plane dendrite and equivalent disc properties are listed in Table 9. The diameter range is limited by Kajikawa's data. The ℓ-δ relation of Auer and Veal is

$$\ell = 2.801 \; \delta^{0.377} \quad . \tag{16}$$

Concentration factors were calculated using the equivalent disc properties. Results are listed in Table 10 and shown in Fig. 13.

---

18. K. O. L. F. Jayaweera, "An Equivalent Disc for Calculating the Terminal Velocities of Plate-Like Ice Crystals," J. Atmos. Sci. 29, 596 (1972).

TABLE 9

PROPERTIES OF PLANE DENDRITIC (Ple) ICE CRYSTALS

Dendrite Diameter (μm)	Thickness (μm)	Mass (μg)	Diameter Of Water Drop Of Equivalent Mass (μm)	Equivalent Disc Density (kg/m^3)	Equivalent Disc Diameter (μm)
500	29.16	0.7356	112	334	341.0
600	31.24	1.0981	128	357	389.4
800	34.82	2.1850	161	402	490.3
1000	37.87	3.6484	191	450	574.1
1500	44.13	8.2800	251	556	720.8
1800	47.27	11.494	280	607	785.4
2500	53.50	∿ 21.129	∿ 343	∿ 712	924.1

TABLE 10

CONCENTRATION FACTORS AT THE LOCKHEED C130 FORMVAR REPLICATOR SLITS FOR PLANE DENDRITIC ICE CRYSTALS (Ple)

Dendrite Diameter (μm)	Concentration Factors C130A 5 kft	C130A 30 kft	C130E 5 kft	C130E 30 kft
500	1.281	1.377		1.214
600	1.302	1.410		1.247
800	1.356	1.439	1.179	1.310
1000	1.388	1.451	1.216	1.372
1500	1.441	1.438	1.292	1.507
1800	1.468	1.416	1.335	1.563
2500	1.490	1.355	1.418	1.623

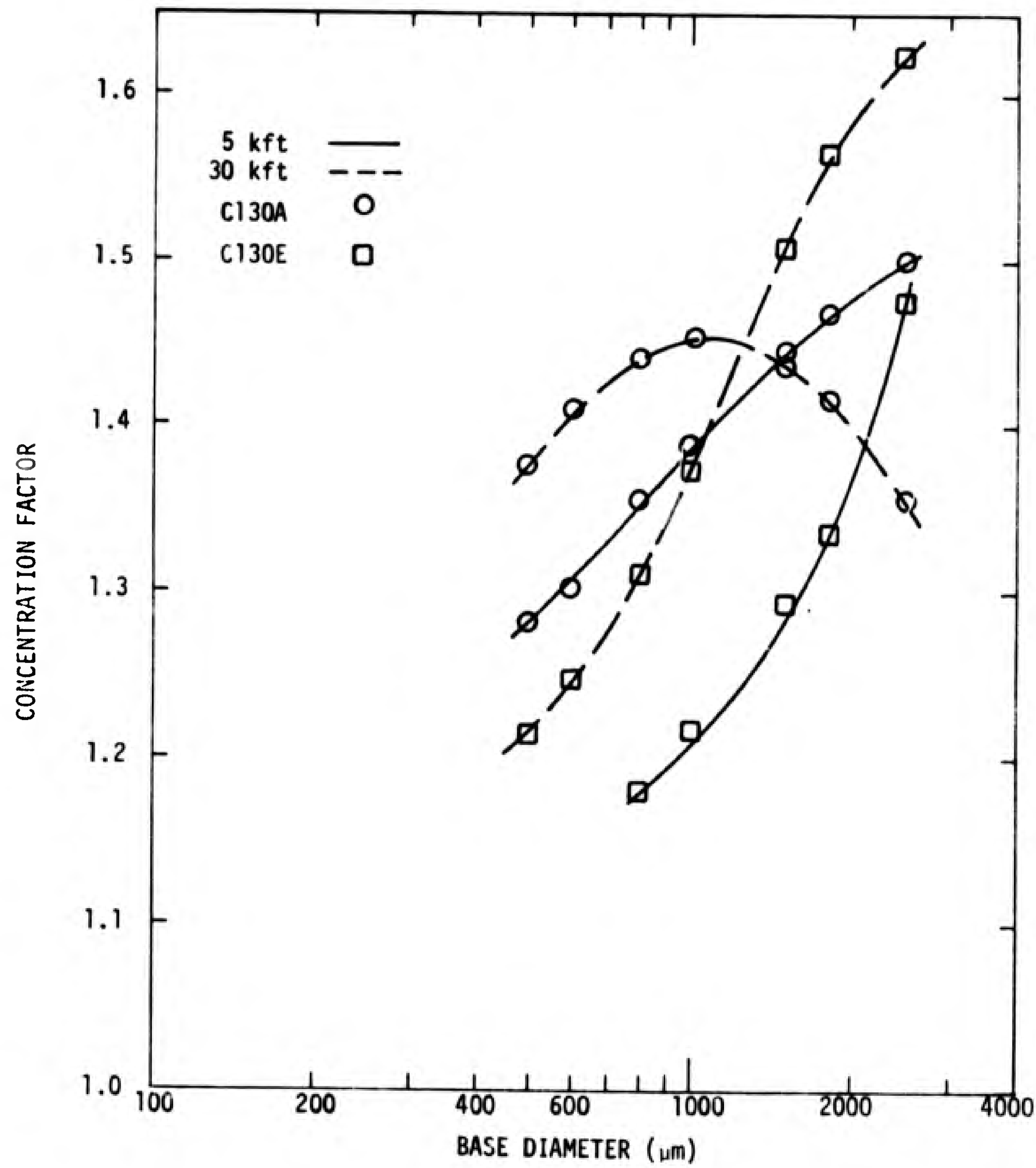

FIGURE 13. Concentration factor vs. base diameter for plane dendrites (Ple) at the Lockheed C130 formvar replicator slits.

AGGREGATES OF UNRIMED RADIATING ASSEMBLAGES OF PLATES, SIDE PLANES, BULLETS AND COLUMNS

Locatelli and Hobbs[19] present observed data and fitted analytical expressions relating settling speed and mass to crystal dimensions for a number of snow and graupel forms. Our interest is in three-dimensional aggregates of crystals, of which the most complete set of data is for aggregates of unrimed assemblages of plates, side planes, bullets and columns. When converted to mks units, Locatelli and Hobbs' expressions are

$$V_T = 11.72\ \delta^{0.41} \tag{17}$$

$$m = 0.01854\ \delta^{1.9} \tag{18}$$

Here δ is "... the diameter of the smallest circle into which the aggregate as photographed will fit without changing density." Thus, in computing crystal volume, we take δ to be the diameter of a sphere; on this basis crystal density is

$$\rho_p = 0.035416\ \delta^{-1.1}\ (\text{kg/m}^3 \text{ and m}). \tag{19}$$

The data were collected in winter in the Cascade Mountains at an average altitude of 1125 m relative to mean-sea-level. Using temperature and pressure from the Geophysics Handbook midlatitude January model atmosphere[20], Eq. (17) can be converted to an expression

---

19. J. D. Locatelli and P. V. Hobbs, "Fall Speeds and Masses of Solid Precipitation Particles," J. Geophys. Res. 79, 2185 (1974).

20. S. L. Valley, editor, Handbook of Geophysics and Space Environments (McGraw-Hill Book Co., New York, 1975). p. 2-14.

for Reynolds number,

$$R_{N,T} = 7.955 \times 10^5 \ \delta^{1.41} \ (\delta \text{ in m}) , \tag{20}$$

and Eq. (18) can be converted to an expression for Best number,

$$B_{N,T} = 1.8571 \times 10^9 \ \delta^{1.9} \ (\delta \text{ in m}) \quad . \tag{21}$$

Substituting Eq. (21) into (20), we obtain

$$R_{N,T} = 0.10524 \ B_{N,T}^{\ 0.742}, \qquad 200 \leq B_{N,T} < 3000 \ . \tag{22}$$

The inverse of Eq. (22) is used to estimate particle drag during trajectory calculations,

$$B_N = 20.78 \ R_N^{\ 1.35}, \qquad 5 \leq R_N < 220 \quad . \tag{23}$$

Aggregate properties are given in Table 11; concentration factor results are listed in Table 12 and plotted in Fig. 14.

DISCUSSION OF CONCENTRATION FACTOR RESULTS

Figs. 15-18 allow comparison of results for the various hydrometeor types. We note that the ice particle curves peak at heavier particle masses than the water drop curves: in the range 200-400 μm diameter melted drops, compared with 100 μm for water drops. We also note that the curves for hexagonal plates and plane dendrites are almost coincident when plotted on a particle mass basis; this is expected in the light of Jayaweera's findings[18] (see p. 33).

Concentration enhancement errors are at most 40-50% at the C130A replicator slit, and 50-60% at the C130E replicator slit. Of course both of these instruments are relatively favorably mounted, with their intake slits well removed from shadow zones and steep concentration gradients.

TABLE 11

PROPERTIES OF AGGREGATES OF UNRIMED RADIATING ASSEMBLAGES OF PLATES, SIDE PLANES, BULLETS AND COLUMNS

Dimension (μm)	Mass (μg)	Density (kg/m^3)	Diameter of Water Drop of Equivalent Mass (μm)
300	3.756	265.7	193
500	9.914	151.5	266
800	24.21	90.3	359
1000	37.0	70.7	413
2000	138.1	33.0	641
3000	298.3	21.1	829

TABLE 12

CONCENTRATION FACTORS AT THE LOCKHEED C130 FORMVAR REPLICATOR SLITS FOR AGGREGATES OF UNRIMED RADIATING ASSEMBLAGES OF PLATES, SIDE PLANES, BULLETS AND COLUMNS

	Concentration Factors			
	C130A		C130E	
Dimension (μm)	5 kft	30 kft	5 kft	30 kft
300	1.312	1.178	1.494	1.509
500	1.253	1.128	1.556	1.401
800	1.197	1.094	1.521	1.308
1000	1.173	1.080	1.499	1.266
2000	1.110	1.047	1.358	1.170
3000	1.083	1.033	1.283	1.128

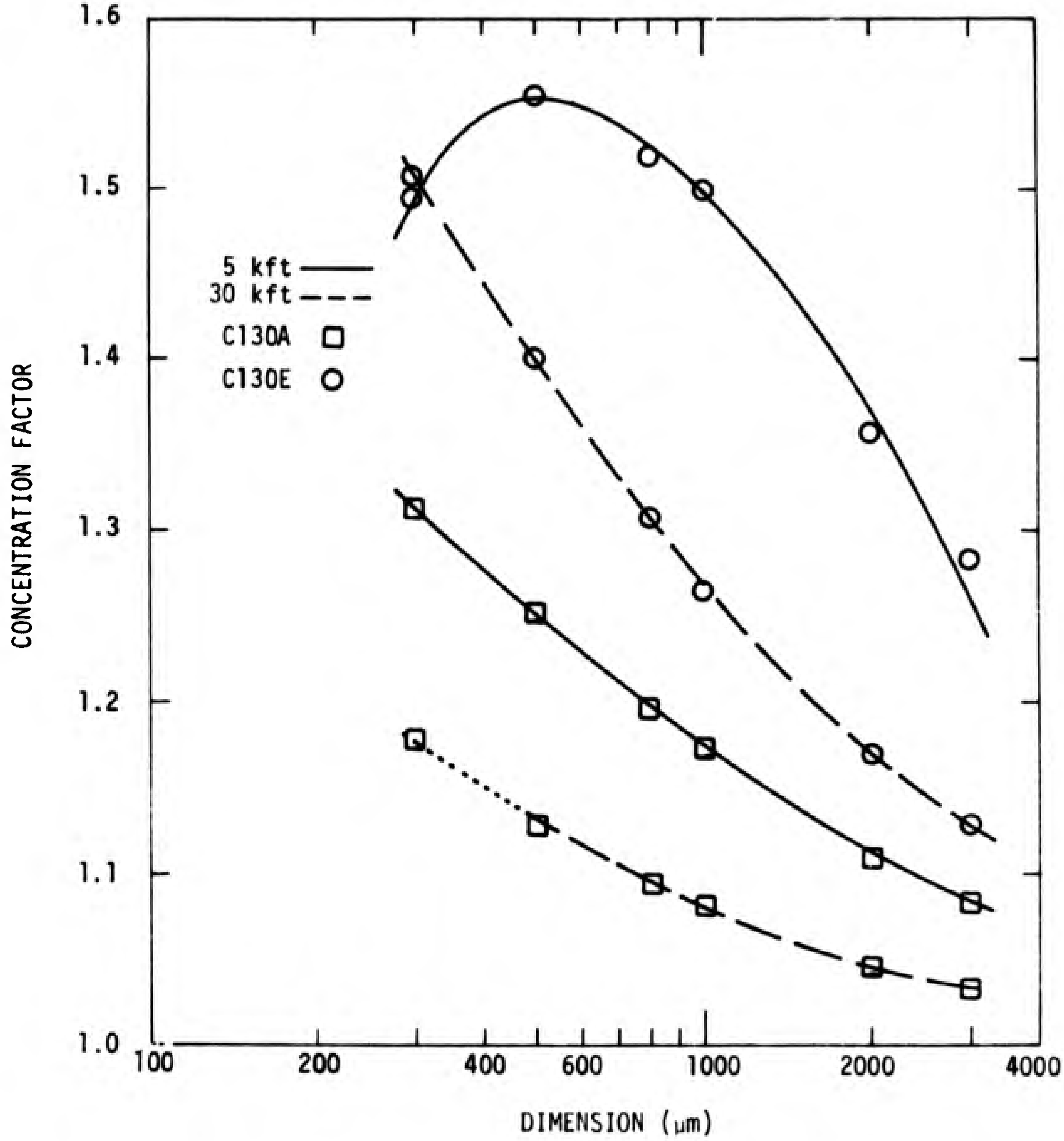

FIGURE 14. Concentration factor vs. aggregate dimension for aggregates of unrimed radiating assemblages at the Lockheed C130 formvar replicator slits.

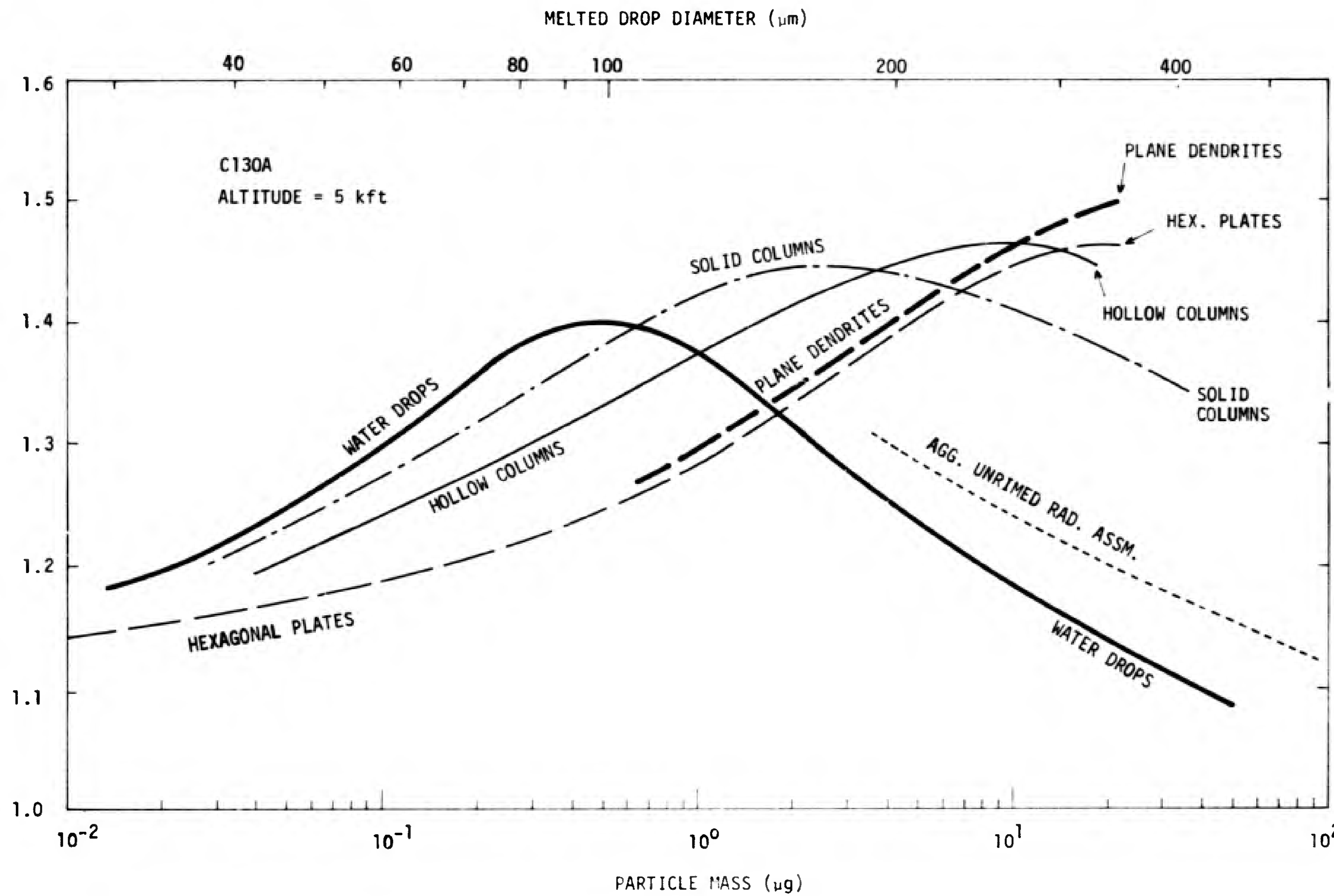

FIGURE 15. Concentration factor vs. particle mass and melted drop diameter for various hydrometeor types at the C130A formvar replicator slit at 5 kft altitude.

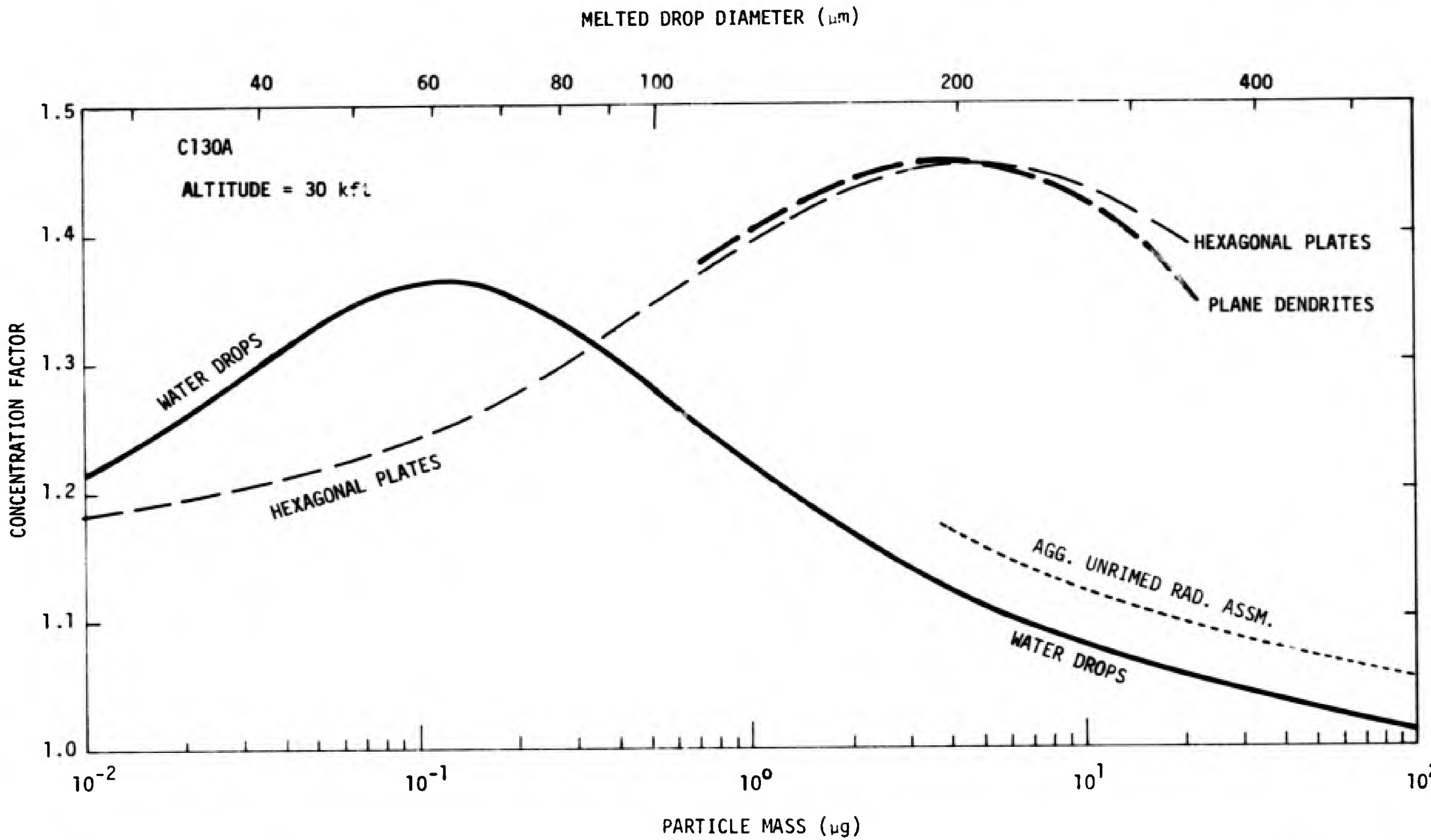

FIGURE 16. Concentration factor vs. particle mass and melted drop diameter for various hydrometeor types at the Lockheed C130A formvar replicator slit at 30 kft altitude.

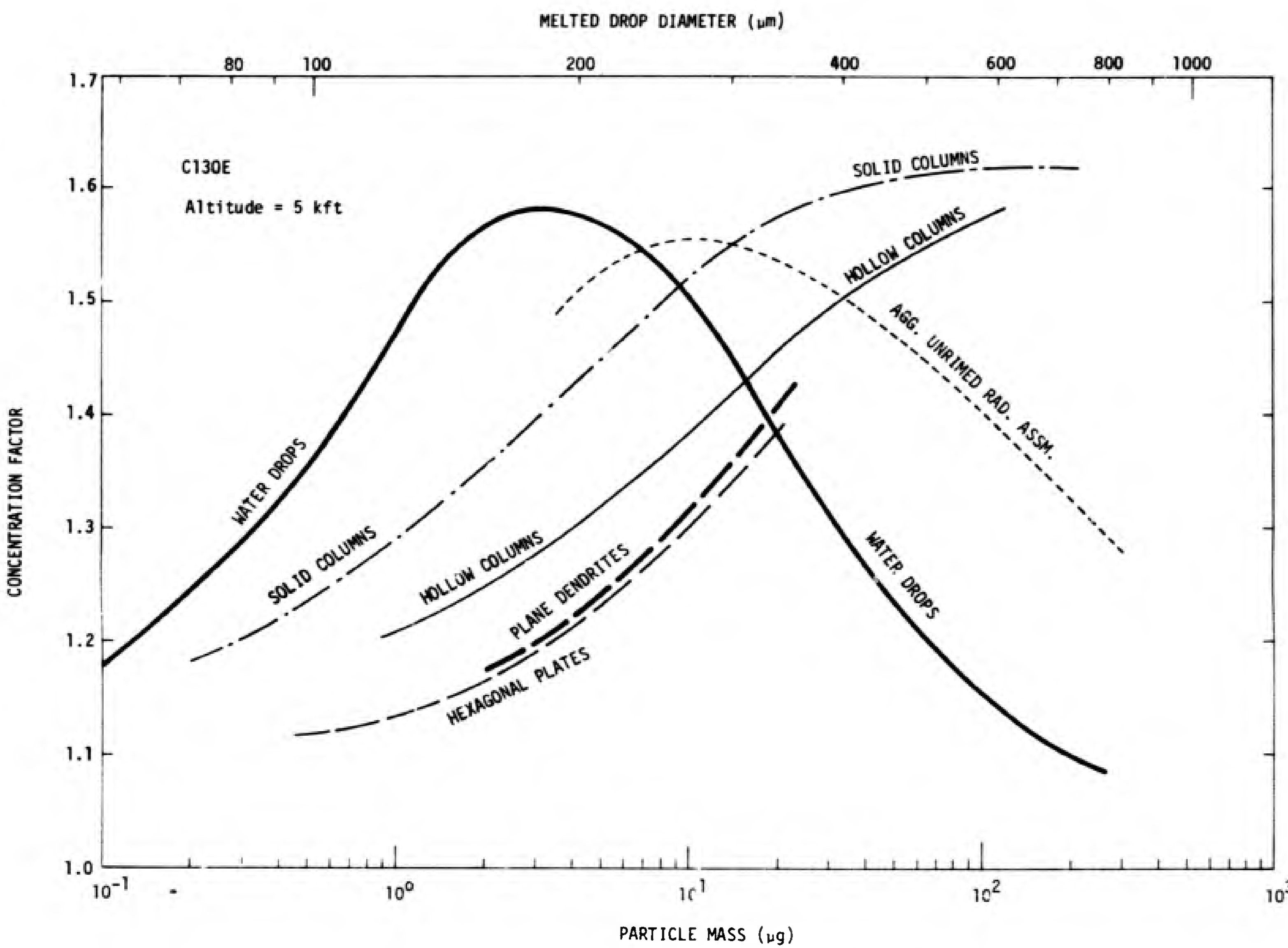

FIGURE 17. Concentration factor vs. particle mass and melted drop diameter for various hydrometeor types at the Lockheed C130E formvar replicator slit at 5 kft altitude.

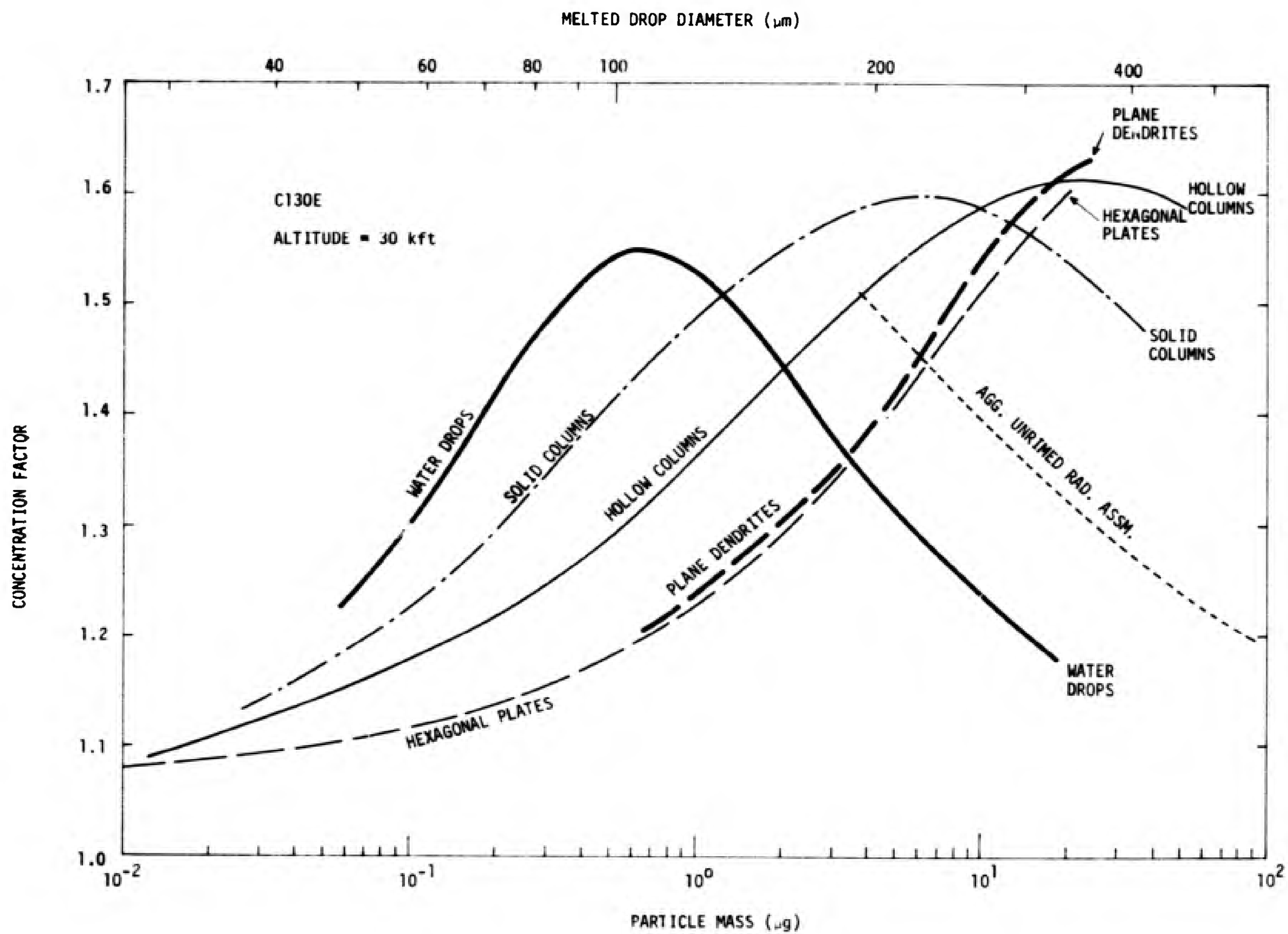

FIGURE 18. Concentration factor vs. particle mass and melted drop diameter for various hydrometeor types at the modified C130E formvar replicator slit at 30 kft altitude.

EFFECTS ON WATER CONTENT MEASUREMENT

In this chapter we use, as an example, the Lockheed C130E formvar replicator results presented above to obtain a notion of how particle concentration distortion may affect overall water content* measurements. For this we use representative hydrometeor size spectra, and we pair our various hydrometeor types with these spectra in reasonable but arbitrary combinations. Concentration factor calculations for more extensive ranges of hydrometeor types and sizes need to be done before observed data can be corrected routinely.

It should be kept in mind that we are dealing with a comparatively favorable case. For situations where the sampling point lies in or near a shadow zone for critical particle sizes**, water content measurements would be indeterminant. Further, we do not include effects of ice particle orientation, which may significantly bias sizing measurements made by linear-array optical particle spectrometers. This latter problem is discussed in Appendix B.

POINT MEASUREMENTS

A clear indication of the effect of concentration distortion on point measurements of water content is obtained by comparison of hydrometeor mass distribution curves with the concentration factor curves. For this purpose, we use hydrometeor size distribution spectra based on the exponential Marshall-Palmer form[21]. In dealing with the

---

* Water content is defined as the mass of water per unit volume of air. Here it is expressed in units g/m^3.

** For example, see concentration factor results for the original C130E formvar replicator, and the Cessna Citation cloud particle spectrometer in Ref. 1.

21. J. S. Marshall and W. McK. Palmer, "The Distribution of Raindrops With Size," J. Meteor. 5, 165 (1948).

spectra, we use the methods and results of Plank, as given in the AFCRL/SAMS series of reports[2,3,4]. Since Plank's descriptions are finely detailed, we suffice here with a cursory review.

For both rain and snow, the distribution of number of particles with size is given by

$$N d\delta = N_0 e^{-\Lambda \delta} d\delta \tag{24}$$

where $N d\delta$ is the number of particles per unit volumne of air in the melted drop diameter range $d\delta$ centered on δ. N_0 and Λ are parameters that vary with hydrometeor type and precipitation rate; they can be expressed as functions of water content for fixed hydrometeor type.

The distribution of hydrometeor mass with size is obtained straightforwardly from (24) as

$$M_\delta d\delta = \frac{\pi}{6} \rho_p N_0 \delta^3 e^{-\Lambda \delta} d\delta , \tag{25}$$

where ρ_p is the density of liquid water. Water content, M, is

$$M = \int_{\delta_{min}}^{\delta_{max}} M_\delta d\delta \quad . \tag{26}$$

Distribution parameters are given in AFCRL/SAMS Report No. 2[2] for $\delta_{min} = 0$, $\delta_{max} = \infty$, and in AFCRL/SAMS Report No. 4[4] for truncated distributions.

Water content is obtained from airplane-collected particle measurements as follows. Particle numbers and sizes are obtained from the instrument as a function of time and location in the cloud. From knowledge of the instrument sampling area the particle flux is computed for a comprehensive set of size classes, and by use of the airspeed, number concentrations for each size class are computed from the flux.

If there is concentration distortion owing to flow about the fuselage, then the true water content is

$$M = \frac{\pi}{6} \rho_p \sum \delta^3 \Delta N_\delta / C_{M,\delta} \quad , \tag{27}$$

where ΔN_δ is measured number concentration of particles in a size class, $C_{M,\delta}$ and δ are median values of concentration ratio and diameter for a size class interval, and the summation is over all size classes.

In Figs. 19-21 are plotted water content distribution frequencies as a function of particle mass (and melted drop diameter) for rain, large snow, and ice crystals. These distributions are truncated at both tails; distribution function parameters are taken from Table G4 of AFCRL/SAMS Report No. 4. Also plotted on these graphs are various concentration factor curves. Flow-caused distortion of water content is proportional to the overlap between the distribution and concentration factor curves.

For rain (Fig. 19), the peaked protions of the curves do not overlap significantly. The particular rain drop distribution plotted is for $M = 0.3 \ g/m^3$; for lighter rainfall, the distribution curve peak shifts to the left and the overlap increases. However, even for light rain, calculations show that we should not expect the flow effect to cause water content excesses greater than about 5%.

For large snow (Fig. 20) the effect should be quite significant for both aggregate snow and plane dendrites, especially the latter. Indeed, if the concentration factor curve for plane dendrites is extropolated to assume the form shown by other hydrometeor types, the overlap should be complete.

For ice crystals (Fig. 21), again we have very substantial overlap. The distribution plotted is for a low value of M ($0.05 g/m^3$), which is commonly exceeded in the upper regions of nimbostratus clouds (see Figs. 22 and 23). For higher water contents, the distribution curve shifts toward the right, and the overlap increases.

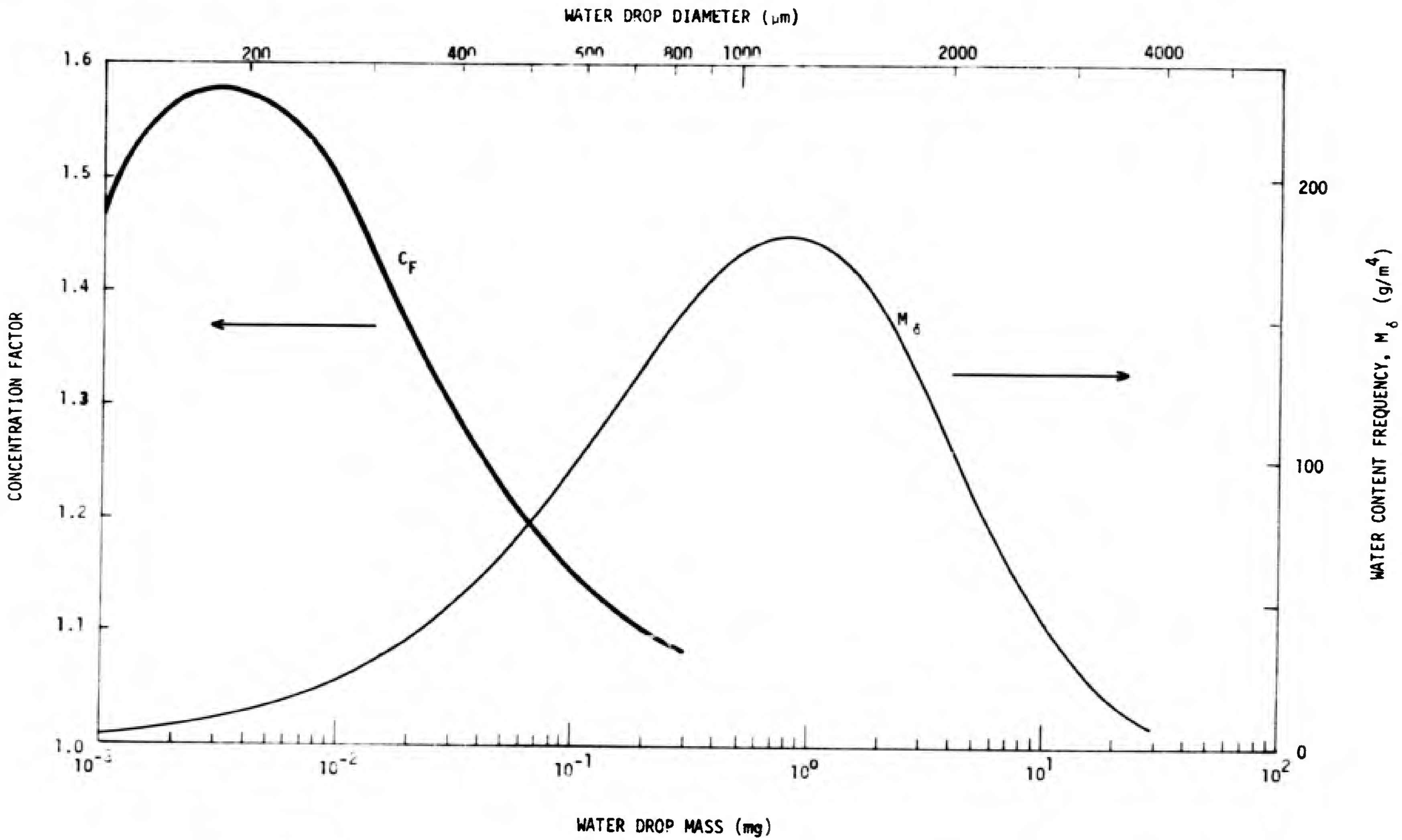

FIGURE 19. Water drop concentration factor and water content frequency vs. drop mass and drop diameter. Concentration factor is for the Lockheed C130E formvar replicator slit at 5 kft altitude. M_δ is for $M = 0.3\ g/m^3$.

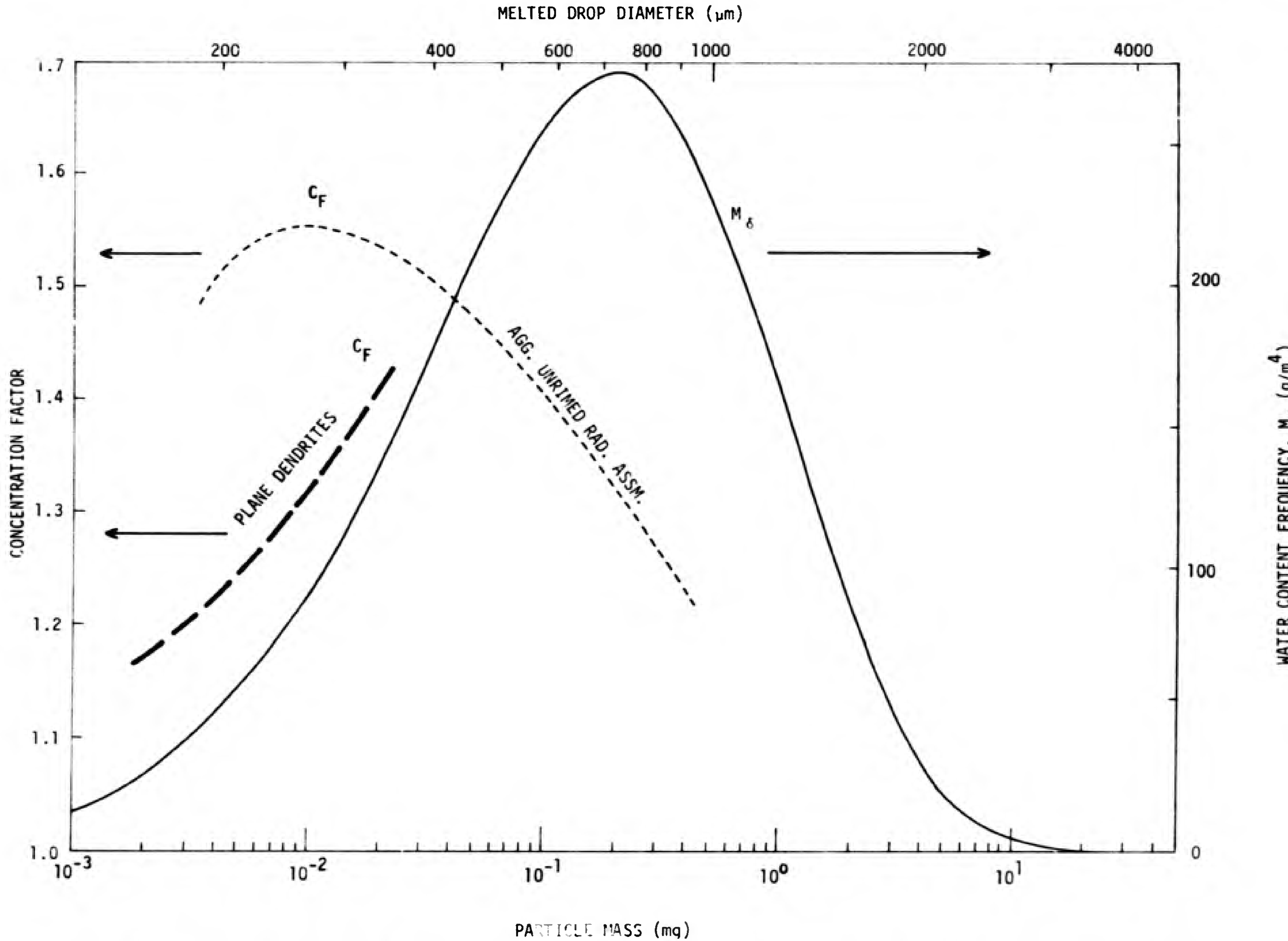

FIGURE 20. Concentration factors for plane dendrites and crystal aggregates, and water content frequency for large snow (LS_3) vs. particle mass and melted drop diameter. Concentration factors are for the Lockheed C130E formvar replicator at 30 kft altitude. M_δ is for $M = 0.3$ g/m^3.

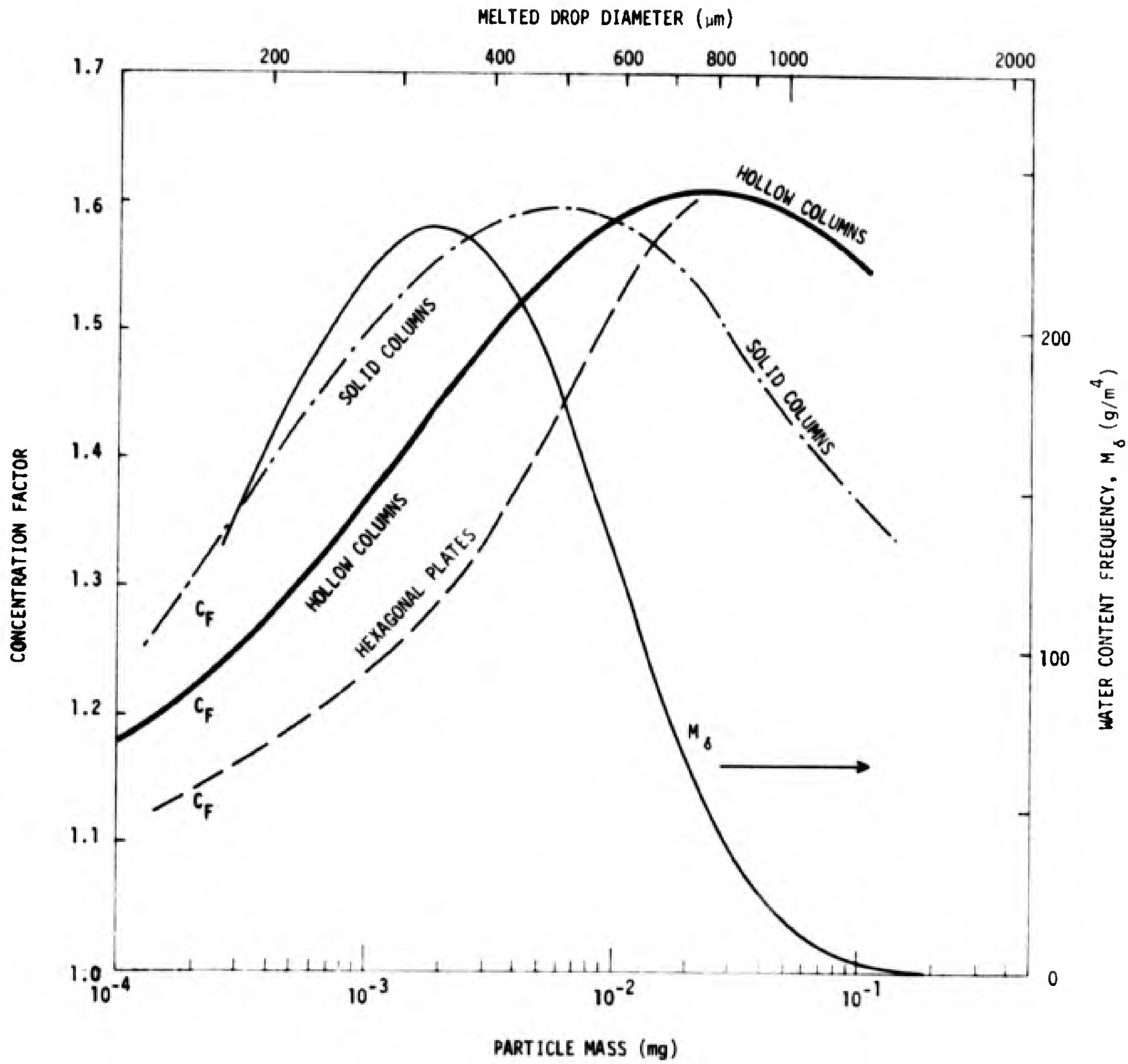

FIGURE 21. Concentration factors for solid columns, hollow columns and hexagonal plates, and water content frequency for ice crystals (C_1) vs. particle mass and melted drop diameter. Concentration factors are for the Lockheed C130E formvar replicator at 30 kft altitude. M_δ is for $M = 0.05$ g/m^3.

For the case of Fig. 21, the hollow and solid column concentration factor curves are sufficiently complete to allow the water content error caused by the flow effect to be calculated. For hollow columns, the water content overestimate would be 43%, and for solid columns, the overestimate would be 48%.

In summary, these data indicate a negligable flow-distortion effect on rain water content. On the other hand for snow and ice, we expect substantial errors; the overestimate in water content being roughly the same percentage as the maximum in the C_M curve.* This is exclusive of any ice particle orientation (see Appendix B) or other effects.

WATER CONTENT INTEGRATED ALONG A MISSILE TRAJECTORY

A missile passing through a cloud is assumed to impact with all water contained in the trajectory tube traced by the missile. The total mass of impacted water per unit area of tube (missile) cros-section, is

$$M_T = \int M dR_s \quad , \tag{28}$$

where dR_s is a differential trajectory arc length, and the integration is along the entire trajectory through the cloud.

Summary tables of "best estimate" spectral distribution and water content data along trajectories of missiles fired from Wallops Island are included in AFCRL/SAMS Reports 3 and 4[3,4], and in additional reports now in preparation. These data are sufficiently detailed that we can combine them with concentration factor results to compute estimates of the effect of flow produced concentration distortion on integrated water content.

---

* Concentration factor is converted to C_M by dividing by v_t (see Eq. (2) and Table 1B).

The AFCRL/SAMS tables contain water content and spectral data at intervals of, for example, 250 meters from the surface to the cloud top. For each altitude increment, the hydrometeor type (rain, large snow, small snow, ice crystal, or transition zone between these types) and total water content in precipitation sized hydrometers (melted drop diameter > 79.43 μm) are given. Also for each altitude increment is given the water content in each of eleven precipitation hydrometeor size classes; these classes range from 79.43 to 12,590 μm melted diameter. The tables are explained fully in the AFCRL/SAMS reports.

For each of the tabulated size classes, we have assigned average concentration ratios, C_M, for the various hydrometeor types. We use C_M values computed at the Lockheed C130E modified replicator slit: at 5 kft for the rain and 30 kft for all of the snow and ice. Pairings of C_M data with the AFCRL/SAMS nydrometeor types are as follows:

AFCRL/SAMS	C_M
rain	water drops
large snow	aggregates of unrimed radiating assemblages
small snow	plane dendrites
ice crystals	solid columns

Wherever necessary the concentration factor curves were extrapolated to provide complete coverage of the particle distribution data.

Of the many missile flights at our disposal we arbitrarily chose two for our calculations: Flight No. Q2-5298 of 17 February 1972 at 1456GMT[3], and Flight No. Q3-6848 of 2 May 1974 at 2035GMT[22]. Results are shown in Figs. 22 and 23. Correct (i.e., reported) and flow-

---

22. V. G. Plank, to be published.

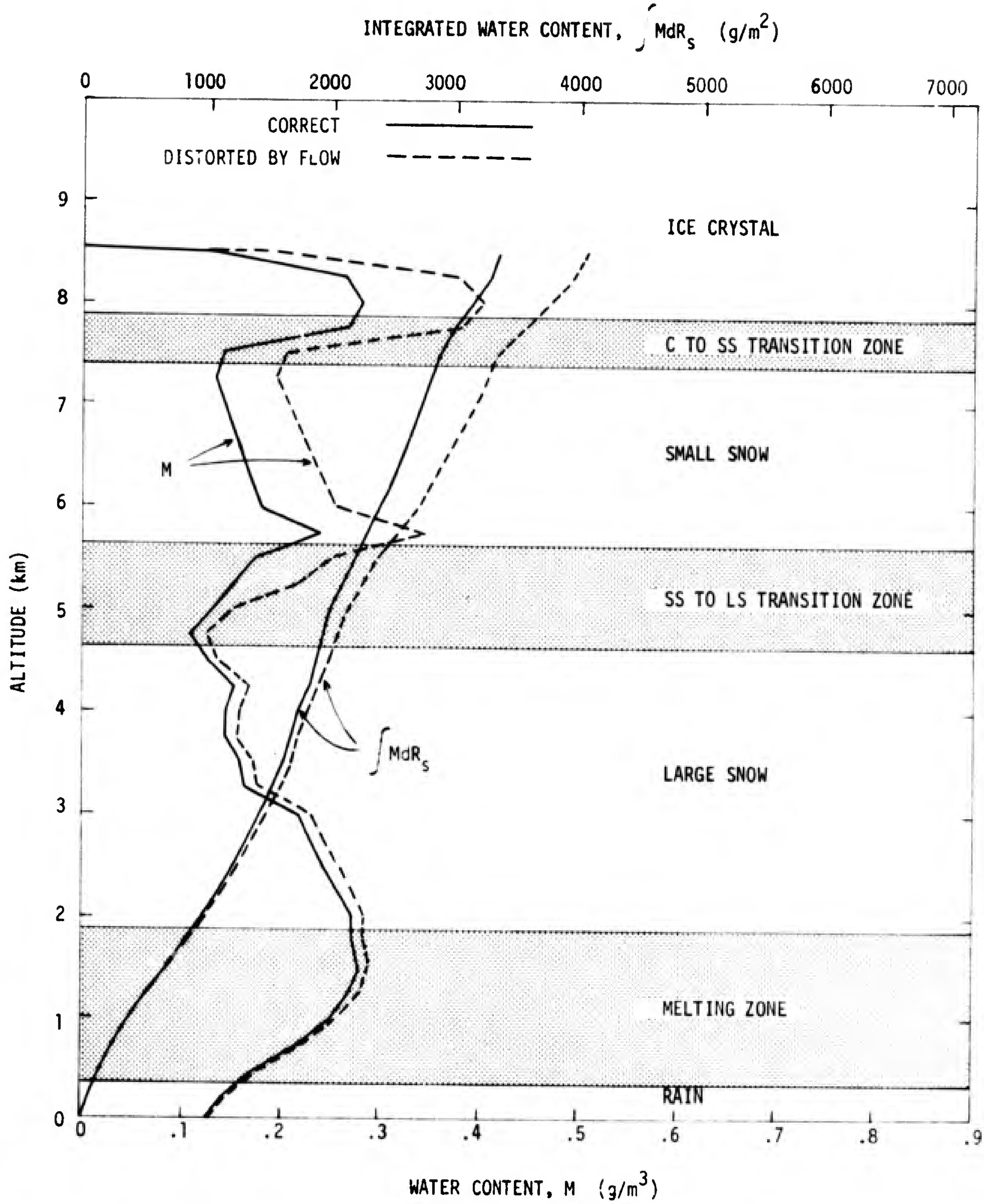

FIGURE 22. Altitude profiles of water content and integrated water content for SAMS missile flight Q2-5298, 17 February 1972 at 1456 GMT, from Wallops Island, Virginia.

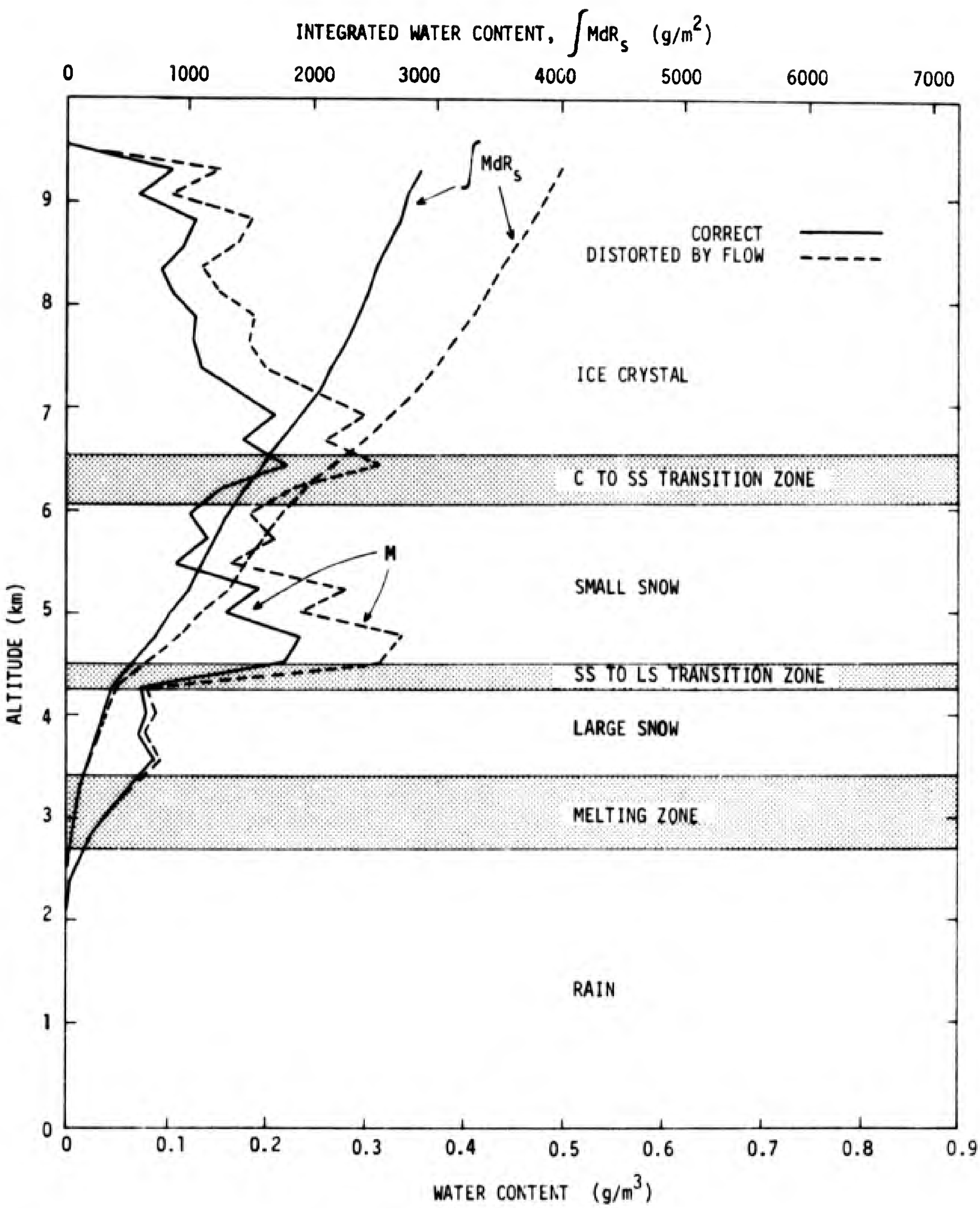

FIGURE 23. Altitude profiles of water content and integrated water content for the SAMS missile flight Q3-6848, 2 May 1974 at 2035 GMT from Wallops Island, Virginia.

distorted profiles of M and $\int MdR_S$ are given. For the case shown in Fig. 22, the profile is dominated by rain and large snow; accordingly there is a relatively small, though still significant, error of 20% in total integrated water content, M_T. For the case of Fig. 23, the profile is dominated by small snow and ice crystals, and we have a 40% error in M_T.

These results suggest that when hydrometeor concentration data are obtained by instruments mounted on airplane fuselages substantial integrated water content errors caused by flow distortion are expected.

SUMMARY AND CONCLUSIONS

Aerodynamic drag equations are developed for plate and plane shaped ice crystals, and for crystal aggregates. These supplement equations reported in Ref. 1 for water drops and ice columns. Comprehensive concentration factor results are reported for the sites of the intake slits of formvar particle replicators mounted on the fuselages of Lockheed C130A and C130E cloud research aircraft.

Using the available concentration factor results for the C130E formvar replicator site as an example, we compute water content measurement errors caused by flow distortion, and we estimate the cumulative effect of such errors on computed total water content seen by missiles in traversing nimbostratus clouds. These calculations use water content and hydrometeor size spectra reported in the AFCRL/SAMS report series. Results indicate negligable error for rain, but quite significant error for snow and ice. For the cases studied, water content errors, for points and for integrations along missile trajectories, of better than 40% can be expected. For cases of unfavorably mounted instruments, where "shadowed zones" prevent collection of hydrometeors of critical sizes, water content measurement is indeterminate.

APPENDIX A. FLOW DISTORTION EFFECTS AT WING-MOUNTED PARTICLE MEASURING INSTRUMENTS

The Lockheed C130 airplanes have modified 450-gallon fuel tank pods slung beneath their left wings. On each pod is mounted: a cloud droplet spectrometer, a precipitation particle spectrometer, and an axial scattering probe, all manufactured by Particle Measuring Systems, Inc. The question has arisen of the effect of air flow around the wing and pod on particle concentrations at the measurement points. We have studied the geometry of the problem via construction of scale drawings of the wing, pod, and sampling instruments. From these drawings, it is apparent that there is no significant flow distortion problem at any of the instruments.

We have included the outboard propeller on the scale drawings to show its proximity to the instruments. This was done to explore the possibility of a propwash turbulence problem. We tentatively conclude that the propeller is sufficiently remote to avoid the problem, but this conclusion lacks quantitative verification.

To construct the scaled drawings we used information from engineering drawings of the airplane, engineering drawings of the pod with instruments mounted, and results of dimensional measurements made on the wing-pod ensemble.

Figures A1 and A2 show the ensemble of wing, pod, propeller, and sampling instruments on the C130 airplanes. Comparison of the positions of pod and samplers relative to the wing, with the streamlines shown in Fig. A3, shows clearly that the airflow around the wing will not significantly influence the flow around the pod and samplers. We conclude that there is no need to pursue this matter further.

There remains the possibility that flow around the pod will influence particle concentrations at the instrument sampling points. The

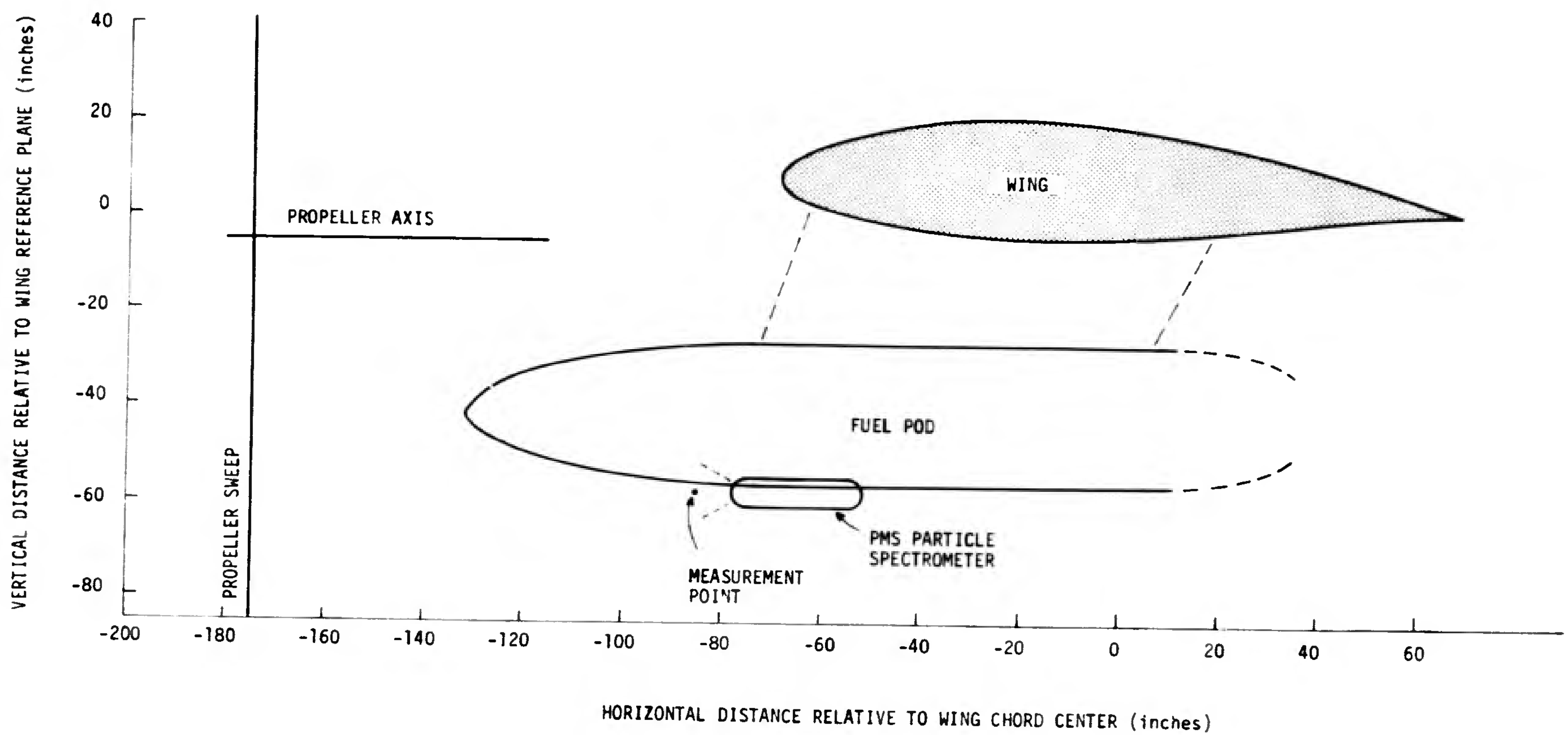

FIGURE A1. Ensemble of wing, fuel pod, hydrometeor sampling instrument and propeller on the C130 airplanes. Vertical plane is parallel to the fuselage axis.

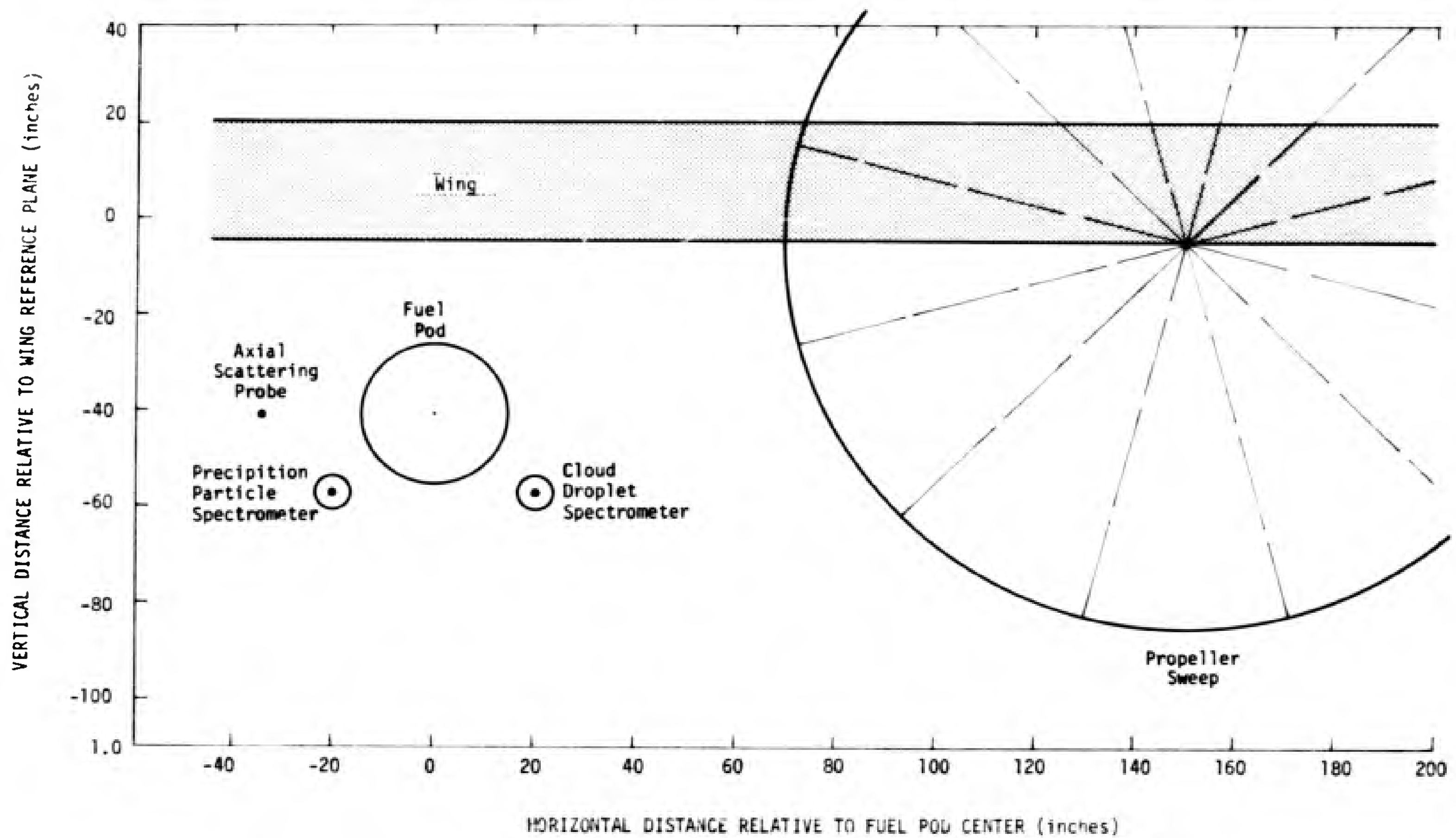

FIGURE A2. Ensemble of wing, fuel pod, hydrometeor sampling points, and propeller on the C130 airplanes. Vertical plane is perpendicular to the fuselage axis.

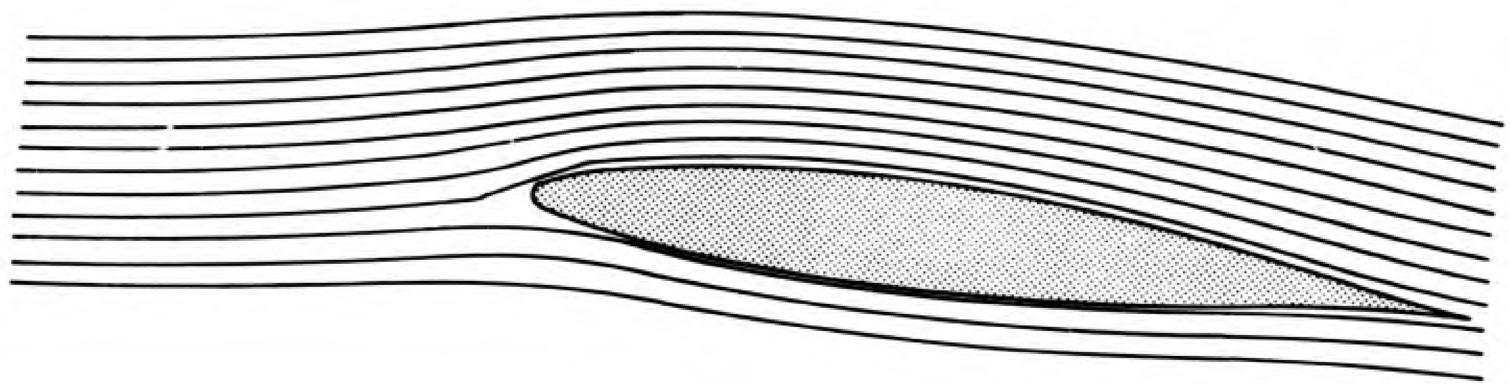

FIGURE A3. Potential flow streamlines around an NACA 65_1 - 212 airfoil at 4^o angle-of-attack.

(S. Kuo-Kai Chai, "Droplet Trajectories Around Aircraft Wing," Thesis, U. Nevada, Reno (November 1973).)

results in Fig. A4* are for an ellipsoid of fineness ratio 2 (major axis/minor axis = 2), whereas the nose of the wing pod is ellipsoidal with fineness ratio 4, with a seven-foot cylindrical section between it and the pod tail section. In spite of these differences in geometry, an indication of the seriousness of the pod flow problem is readily obtained. As shown in Fig. A2, the two instruments closest to the pod have their measurement points at distances of 0.8 x (pod radius) from the pod surface. In Fig. A4, this results in concentration factor enhancement of less than 10%. We conclude that there is no need to pursue this matter further.

With regard to the effect of the propeller, we note from Fig. A1 that the propeller is about 9 feet forward of the particle spectrometers, and from Fig. A2 that its closest distance in the transverse plane is about 6 feet. Propeller vortex tubes are known to contract as they leave the blade tips. Thus, we can be assured that the sampling instruments are not directly in the propwash turbulence. Moreover it appears that the sampling points are sufficiently remote from the propwash that there probably is little effect. However, we have not studied the propeller problem quantitatively, so that these opinions are intuitive rather than factual.

---

* Fig. A4 is a recalculation of a graph obtained by Whitten(23) via interpolation of NACA calculated trajectory data.

23. R. P. Whitten, "An Investigation of Some Aerodynamic Factors Affecting Meteorological Instrument Readings on a C130A Research Aircraft," Allied Research Assoc., Inc., AFRD TN-60-454 (15 May 1960). Fig. 11.

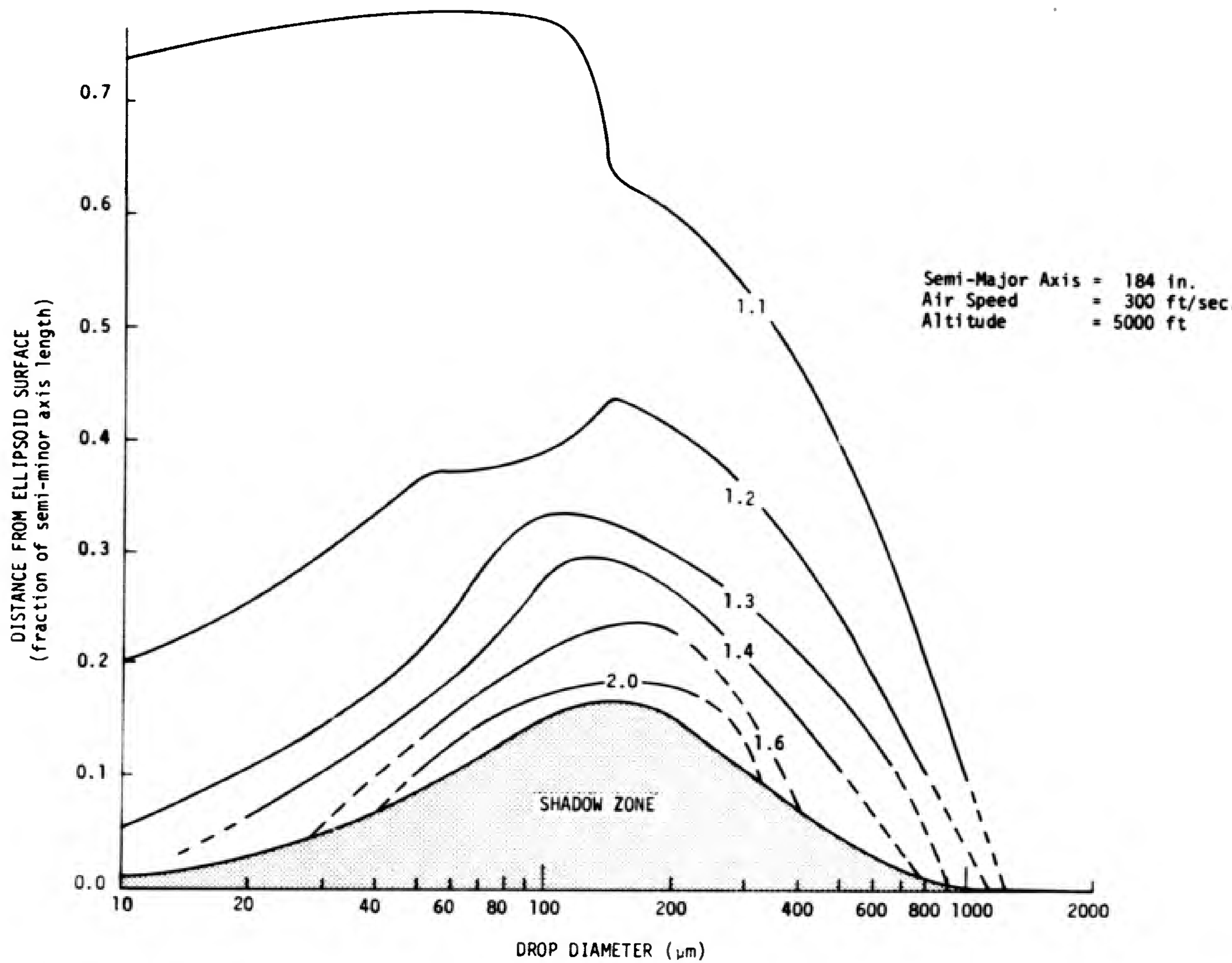

FIGURE A4. Water drop concentration factor contours along extension of minor axis of ellipsoid of fineness ratio 2.

APPENDIX B. EFFECT OF ICE CRYSTAL ORIENTATION ON SIZE MEASUREMENT

In Ref. 1 and in our discussion of the settling of plates above, we present evidence to support the hypothesis that, except for the smallest and largest crystals, we can expect columnar and planar ice crystals to orient with their largest dimensions perpendicular to the drag force vector. In free-fall settling this means that columns orient with their long axes horizontal and planar crystals orient with their faces downward. The question arises as to whether these orientations are maintained at sampling points near airplane fuselages. If not, then interpretation of linear-array optical particle spectrometer[24] results may be erroneous since the spectrometers record projections of the crystal dimensions on their linear optical arrays. To shed some light on this problem we have calculated drag vector angles at sampling points during some of the concentration factor calculations discussed above.

Figure B1 defines the drag vector angles. The angles Ω and γ can be used to indicate departure from the free-fall settling orientation. They are defined in terms of the drag vector direction cosines as

$$\Omega = \tan^{-1} (\cos \beta / \cos \alpha) \qquad \text{(B1)}$$

$$\gamma = \cos^{-1} (\cos \gamma) \quad , \qquad \text{(B2)}$$

where the direction cosines are computed from the drag vector components.

---

24. R. G. Knollenberg, "The Optical Array: An Alternative to Scattering or Extinction for Airborne Particle Size Determination," J. Appl. Meteor. 9, 86 (1970).

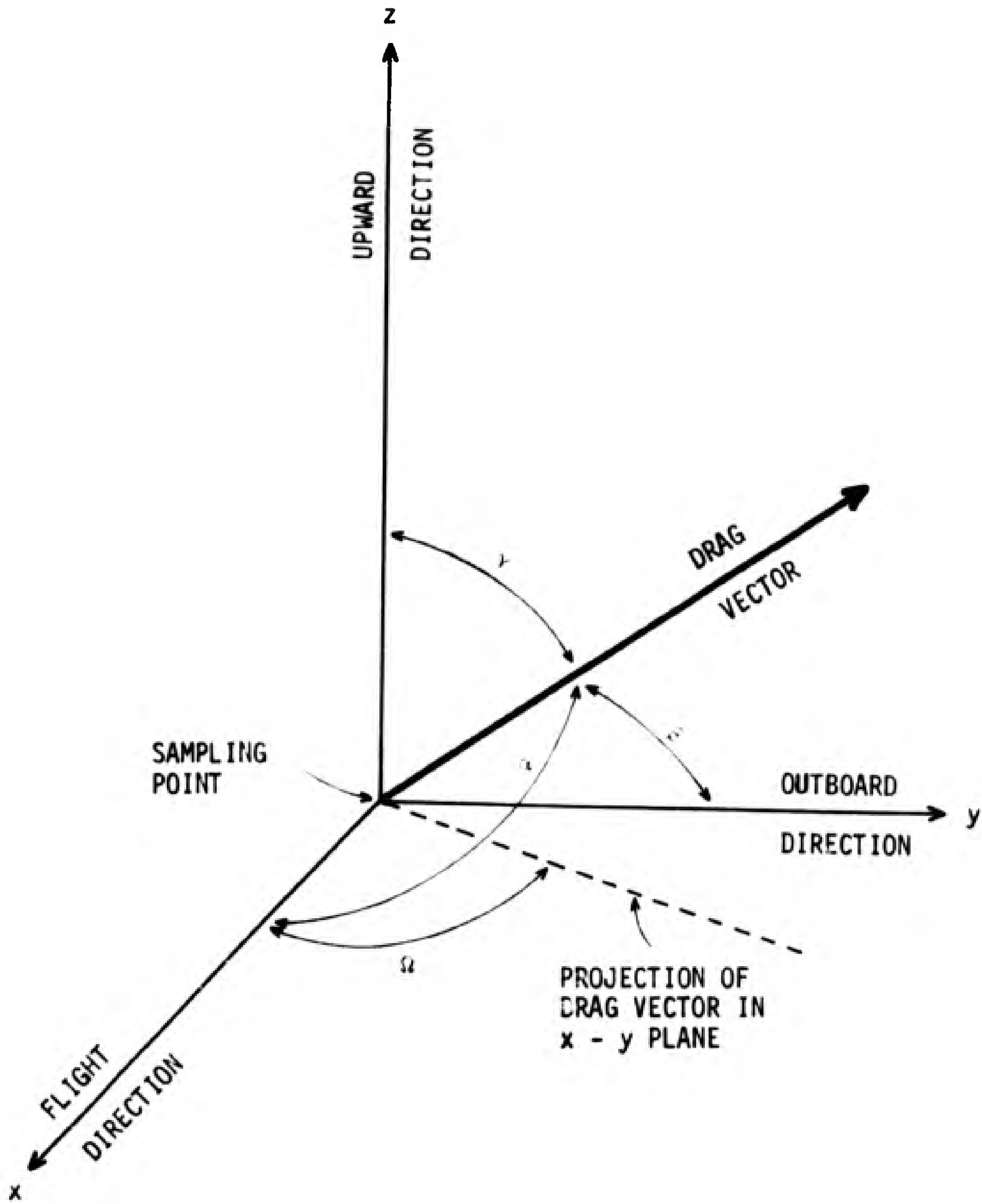

FIGURE B1. Geometrical definition of hydrometeor drag vector direction angles at a hydrometeor sampling point near an airplane fuselage. For undisturbed free-fall settling, the drag vector points vertically.

For a crystal in stable free-fall, both γ and Ω are zero.

Table B1 indicates how far this condition is from being realized for plate crystals. For a thin plate, the dimension, $\delta_{\perp}$, recorded by a linear device arrayed parallel to the y axis is

$$\delta_{\perp} = \delta|\sin \beta| \quad . \tag{B3}$$

For columnar crystals we have a combination of two projections. First we have the drag vector tilted relative to the perpendicular as described above, and we take the long axis of the column to be perpendicular to the drag vector. Additionally, we assume that the column axis can assume any orientation in the plane normal to the drag vector. In Appendix C of Ref. 1 we show that the ensemble mean dimension projected along this plane is

$$< \nabla > = \frac{2}{\pi} (\delta+\ell) \quad . \tag{B4}$$

The overall mean projected dimension, presumably as recorded by the linear optical array, is

$$< \nabla >_{\perp} = < \nabla > |\sin \beta| \quad . \tag{B5}$$

Illustrative results for solid columns are listed in Table B2.

For both plates and columns these results indicate that very substantial errors can occur. Underestimation errors in the measurement of maximum crystal dimensions in excess of factors of two can be expected for the larger crystals.

TABLE B1

ORIENTATION ANGLES OF HEXAGONAL PLATES AT THE LOCKHEED C130E FORMVAR REPLICATOR SLIT AT 30 kft ALTITUDE

Plate Diameter (μm)	Orientation Angles (degrees) Ω	β	γ	Projection Of Plate Diameter On y Axis (μm)
50	-151	117	69	45
100	-149	118	70	88
200	-144	123	69	168
300	-139	129	69	232
400	-132	134	68	290
500	-127	138	68	336
600	-122	142	67	371
800	-111	149	66	415
1000	-103	153	65	460

TABLE B2

ORIENTATION ANGLES OF SOLID COLUMNS AT THE LOCKHEED C130E FORMVAR REPLICATOR SLIT AT 30 kft ALTITUDE

Column Length (μm)	$<\nabla>$ (μm)	Orientation Angles (degrees) Ω	β	γ	Overall Projected Dimension $<\nabla>\lvert\sin\beta\rvert$
50	54.6	-145	123	70	46
100	107.1	-126	138	68	71
190	180.	-113	148	66	97
500	410.	- 98	154	65	182
700	551.	- 93	154	64	244
1000	762.	- 87	152	62	354
2000	1440.	- 79	147	58	792
4000	2769.	- 70	140	54	1781

APPENDIX C. GLOSSARY OF SYMBOLS

A	cross-sectional area of particle flux tube in the free-stream (m^2)
A_p	area of particle projected in its direction of motion (m^2)
A_t	cross-sectional area of a particle flux tube in the target plane (m^2)
B_N	Best number
C_D	drag coefficient
C_F	concentration factor (Eq. (1))
C_M	particle concentration ratio (Eq. (2))
d	differential operator
F	particle flux in the free-stream (kg/(m^2-sec))
F_N	Froude number
F_t	particle flux at a target point (kg/(m^2-sec))
g	gravity acceleration constant (9.8 m/sec^2)
$\vec{g}$	acceleration of gravity (m/sec^2)
ℓ	ice column length or plate thickness (μm or m)
L	characteristic dimension of an airplane (m, feet or inches)
m	particle mass (μg or kg)
$\dot{m}$	mass transfer rate through a particle flux tube (kg/sec)

M	water content (g/m^3)
M_T	total integrated water content along a missile trajectory (g/m^2)
M_δ	water content for particles of melted diameter δ per melted drop diameter (g/m^4)
N	number of particles per volume of air per melted drop diameter (m^{-4})
N_0	constant in the Marshall-Palmer form of hydrometeor size distribution equation (m^{-4})
P	ratio of Best to Reynolds numbers ($P = B_N/R_N$)
P_T	ratio of Best to Reynolds numbers for terminal particle settling
R_N	Reynolds number
R_s	missile trajectory arc length (m)
t	time (sec)
v_{fx}, v_{fy}, v_{fz}	air velocity components (dimensionless)
v_{px}, v_{py}, v_{pz}	particle velocity components (dimensionless)
v_t	air speed at the target point (dimensionless)
v_T	terminal settling speed of a particle (dimensionless)
V	free-stream air speed (m/sec)

$\vec{V}_f$	air velocity (m/sec)
$\vec{V}_p$	particle velocity (m/sec)
V_t	air speed at the target point (m/sec)
V_T	terminal settling speed of a particle (m/sec)
x,y,z	space coordinates (dimensionless)
α,β,γ	direction cosine angles of a drag force vector
ρ	air density (kg/m^3)
ρ_p	particle density (kg/m^3)
τ	time (dimensionless)
δ	particle dimension (μm or m)
η	air viscosity (kg/(m-sec))
Ω	drag force vector angle as defined in Fig. B1.
γ	projected dimension of an ice column (μm)(Eq. (11)).

REFERENCES

1. H. G. Norment and R. G. Zalosh, "Effects of Airplane Flow Fields on Hydrometeor Concentration Measurements," Mt. Auburn Research Associates, AFCRL-TR-74-0602 (6 December 1974).

2. V. G. Plank, "Hy ometeor Parameters Determined From the Radar Data of the SAMS R . Erosion Program. AFCRL/SAMS Report No. 2," AFCRL-TR-74-0249, Environmental Research Papers, No. 47? (4 June 1974).

3. V. G. Plank, "Liquid-Water-Content and Hydrometeor Size-Distribution Information for the SAMS Missile Flights of the 1971-72 Season at Wallops Island, Virginia. AFCRL/SAMS Report No. 3," AFCRL-TR-74-0296, Special Reports, No. 178 (2 July 1974).

4. V. G. Plank, "Liquid-Water-Content and Hydrometeor Size-Distribution Information for the SAMS Missile Flights of the 1972-73 Season at Wallops Island, Virginia. AFCRL/SAMS Report No. 4," in preparation.

5. F. T. Krogh, "Variable Order Integrators for Numerical Solution of Ordinary Differential Equations," Jet Propulson Lab Technology Utilization Document No. CP-2308 (November 1970).

6. J. L. Hess and A. M. O. Smith, "Calculation of Non-Lifting Potential Flow About Arbitrary Three-Dimensional Bodies," McDonnell Douglas Report E. S. 40622 (15 March 1962). AD-282 255.

7. J. L. Hess and A. M. O. Smith, "Calculation of Potential Flow About Arbitrary Bodies," in Progress in Aeronautical Sciences, Vol. 8, edited by D. Kuchemann (Pergamon Press, New York, 1967).

8. F. A. Woodward, "Analysis and Design of Wing-Body Combinations at Subsonic and Supersonic Speeds," J. Aircraft 5, 528 (1968).

9. J. Hallett, R. W. Hanaway, and P. B. Wagner, "Design and Construction of a New Cloud Particle Replicator for Use on a Pressurized Aircraft," Desert Research Institute, Reno, Nevada, AFCRL-72-0410 (31 May 1972). AD-753 091.

10. H. Wadell, "The Coefficient of Resistance as a Function of Reynolds Number for Solids of Various Shapes," J. Franklin Inst. 217, 459 (1937).

11. K. O. L. F. Jayaweera and B. J. Mason, "The Falling Motions of Loaded Cylinders and Discs Simulating Snow Crystals," Quart. J. Roy. Meteor. Soc. 92, 151 (1966).

Preceding page blank

12. M. Kajikawa, "A Model Experimental Study on the Falling Velocity of Ice Crystals," J. Meteor, Soc. Japan 49, 367 (1971).

13. W. W. Willmarth, N. E. Hawk, and R. L. Harvey, "Steady and Unsteady Motions and Wakes of Freely Falling Disks," The Physics of Fluids 7, 197 (1964).

14. R. List and R. S. Schemenauer, "Free-Fall Behavior of Planar Snow Crystals, Conical Graupel and Small Hail," J. Atmos. Sci. 28, 110 (1971).

15. K. O. L. F. Jayaweera and R. E. Cottis, "Fall Velocities of Plate-Like and Columnar Ice Crystals," Quart. J. Roy. Meteor. Soc. 95, 703 (1969).

16. M. Kajikawa, "Measurement of Falling Velocity of Individual Snow Crystals," J. Meteor. Soc. Japan 50, 577 (1972).

17. A. H. Auer and D. L. Veal, "The Dimensions of Ice Crystals in Natural Clouds," J. Atmos. Sci. 27, 919 (1970).

18. K. O. L. F. Jayaweera, "An Equivalent Disc for Calculating the Terminal Velocities of Plate-Like Ice Crystals," J. Atmos. Sci. 29, 596 (1972).

19. J. D. Locatelli and P. V. Hobbs, "Fall Speeds and Masses of Solid Precipitation Particles," J. Geophys. Res. 79, 2185 (1974).

20. S. L. Valley, editor, Handbook of Geophysics and Space Environments (McGraw-Hill Book Co., New York, 1975). p. 2-14.

21. J. S. Marshall and W. McK. Palmer, "The Distribution of Raindrops With Size," J. Meteor. 5, 165 (1948).

22. V. G. Plank, to be published.

23. R. P. Whitten, "An Investigation of Some Aerodynamic Factors Affecting Meteorological Instrument Readings on a C130A Research Aircraft," Allied Research Assoc., Inc., AFRD TN-60-454 (15 May 1960). Fig. 11.

24. R. G. Knollenberg, "The Optical Array: An Alternative to Scattering or Extinction for Airborne Particle Size Determination," J. Appl. Meteor. 9, 86 (1970).